The BICEP Array Housekeeping System and the Calibration of the Daughter Cards

A thesis submitted to the Graduate School of the University of Cincinnati for the degree of Masters of Science in the Department of Physics of the McMicken College of Arts and Sciences.

By: Kyle Weeks

August 2022

Supervised by and Committee Member: Dr. Colin Bischoff, Physics
Committee Member: Dr. Conor Henderson, Physics
Committee Member: Dr. Rohana Wijewardhana, Physics

Contents

List of Figures

1 Cosmological Background

Cosmology is the study of the Universe as a whole; how the Universe originated to how it evolved to its current state today. The leading theory for the origin of the Universe is the Big Bang Theory. The quick story is that the Universe began from an explosion. This resulted in a state with extreme temperatures and densities. The Universe started to expand and cool which allowed subatomic particles, atoms and molecules to form. As these particles formed and became more abundant, they formed physical structures like stars from gravity. Well, as fascinating as this short story is, it doesn't provide the details or mechanics of how we experience the Universe as it is.

Cosmologist want to study the origins of the Universe and want to explore this evolution. The Big Bang Theory was one attempt constructed to describe this evolution of the observable Universe. The Big Bang Theory became the leading theory for the origin of the Universe when the Cosmic Microwave Background (CMB) was discovered. The CMB provided direct evidence that the Universe was once hot, dense and homogeneous. The ΛCDM model or the Standard Model is a rendition of the Big Bang theory that seems to predict some properties and physics of the Universe reasonably well. The three main ingredients of the Universe, according to the ΛCDM, is the cosmological constant (Λ) relating to dark energy, cold dark matter (CDM) and ordinary matter. The standard model accounts for observables like the accelerating expansion of the Universe and the structure of the CMB. The theory of Inflation was created to deal with the incompatibilities with the Big Bang Theory like the horizon problem, the flatness problem, and the magnetic monopole problem. Inflation is helpful because it provides a solution to the problems mentioned but is also, compatible with ΛCDM model. But, Inflation is an incomplete theory and requires more insight. The BICEP Program measures specific polarizing effects in the CMB known as B-Modes that are a result of Primordial Gravitational Waves (PGWs) to support the theory of Inflation. However, the BICEP Program has set upper limits on PGWs and has measure B-mode polarization from sources like Galactic foregrounds and lensing of the CMB.

In Chapter 1, I will discuss a simplified version of modern cosmology to understand the theoretical importance of this thesis and to provide the information of to understand the importance of the BICEP Program as a whole. In Chapter 2, I will provide an overview of the BICEP Program, the architecture of BICEP Array and the process in which BICEP Array functions. In Chapters 3, 4, and 5, I will provide a detailed analysis of the calibration of individual parts associated with the Housekeeping System and the BICEP Array.

1.1 Modern Cosmology

The Cosmological Principle is a fundamental principle of cosmology which states that on a large scale, the Universe is both spatially homogeneous and isotropic.[2] Obviously, there are local differences but at large scales this principle holds. The implications to the Cosmological Principle is that there are no 'special' positions in the space; as every other part of the Universe would be similar to our position in the Universe. Therefore, there is no center or edge to the Universe as every position must have the same view point in every direction at any point in space. So, the laws of physics in our spot in the Universe hold at any location. This is important because it lets us assume that the area of space that we can observe and are located in is representative of the entire Universe.

We can use the Cosmological Principle to describe the dynamics of the Universe. The Einstein Field Equation (EFE) uses general relativity to relate the distribution of matter within the Universe to the geometry of space-time. Meaning, EFE tells us how space-time evolves in the presences of matter and how matter behaves in the presences of curved space-time. EFE is written as

$$R_{\mu\nu} - \frac{1}{2}Rg_{\mu\nu} + \Lambda g_{\mu\nu} = \frac{8\pi G}{c^4}T_{\mu\nu} \tag{1}$$

where,

$$R_{\mu\nu} = the\ Ricci\ Tensor$$
$$R = the\ Ricci\ Scalar$$
$$g_{\mu\nu} = the\ metric\ tensor$$
$$\Lambda = the\ cosmological\ constant$$
$$G = Newton's\ Constant$$
$$T_{\mu\nu} = the\ Stress - Energy\ Tensor$$

Applying the Cosmological Principle to the EFE in Equation 1, we get the Friedmann-Roberson Walker metric shown as

$$ds^2 = c^2dt^2 - a^2(t)(\frac{dr^2}{1-kr^2} + r^2d\theta + r^2sin^2(\theta)d\phi^2) \tag{2}$$

Where c^2dt^2 is the temporal component and the second term on the right hand side contains the spatial component in polar coordinates. k is a constant that represents curvature of the spatial components of the Universe. k can have three values -1, 0 and 1. For $k = -1$ the universe is spatially open with a hyperbolic shape and is known as Negative Curvature. For $k = 0$ the universe is flat with a no Curvature. For $k = 1$ the universe is spatially closed with a spherical shape and is known as Positive Curvature. $a(t)$ is the scale factor that describes how the spatial components of the metric grow as a function of time. Now, applying the FRW metric in Equation 2 to the EFE in Equation 1, results in the Friedmann Equations. The assumption made to do this is to apply a perfect fluid which gives a specific Stress-Energy Tensor ($T_{\mu\nu}$). By using only the 00 component or the solely time component, we can derive the first Friedmann Equation shown as

$$H^2 = \frac{\dot{a}^2(t)}{a^2(t)} = \frac{8\pi G\rho}{3} - \frac{kc^2}{a^2} \tag{3}$$

where,

$$H = the\ Hubble\ Parameter$$
$$G = Newton's\ Constant$$
$$\rho = the\ mass - energy\ density$$
$$k = the\ spatial\ curvature\ Constant$$

Equation 3 tells us about the expansion rate (H^2) of the Universe.

The second Friedmann Equation can be obtained by adding the spacial components of the EFE to Equation 3. Thus, the second Friedmann Equation is expressed by

$$\dot{H} + H^2 = \frac{\ddot{a}(t)}{a(t)} = \frac{-4\pi G}{3}(\rho + \frac{3p}{c^2}) \tag{4}$$

where p is the pressure term from the Stress-Energy Tensor. This equation describes the acceleration of the Universe in terms of mass-energy density and pressure.

From the FRW metric where, the Universe is isotropic and filled with a perfect fluid, we can derive an equation of state where the energy density is associated to the scale factor. The scale factor is written as

$$\rho \propto a^{-3(1+w)} \tag{5}$$

where $w = \frac{p}{\rho}$. w can have any value. However, the Standard Model presents three specific values -1, 0, and $\frac{1}{3}$.[2] For $w = -1$ is for the cosmological constant (Λ), $w = 0$ is for non-relativistic particles like matter, and $w = \frac{1}{3}$ is for relativistic particles like radiation. Applying each w value into Equation 5 gives

$$\rho \propto a^0 \tag{6}$$

$$\rho \propto a^{-3} \tag{7}$$

$$\rho \propto a^{-4} \tag{8}$$

Each of these results tells us how each type of matter density scales with an expanding Universe. We can derive the Critical Density of a spatially flat Universe. The Critical Density is the average density of matter for the Universe where the Universe would no longer expand. The Critical Density is derived as

$$\rho_c = \frac{3H^2}{8\pi G} \tag{9}$$

We can write a Density Parameter which is the ratio of the density at current day to the Critical Density shown as

$$\Omega \equiv \frac{\rho_0}{\rho_c} \tag{10}$$

The Density Parameter determines the shape of the Universe. If $\Omega = 1$, then the Universe is spatially flat. This occurs when observed density is equal to the Critical Density. If the observed density is less than the Critical Density ($\Omega < 1$) then the Universe is negatively curved. If the observed density is greater than the Critical Density ($\Omega > 1$) then the Universe is positively curved. We can now rewrite the first Friedmann Equation (Equation 3) in terms of the Density Parameter and the energy density:

$$\frac{H^2}{H_0^2} = \Omega_{0,R}a^{-4} + \Omega_{0,M}a^{-3} + \Omega_{0,k}a^{-2} + \Omega_{0,\Lambda} \tag{11}$$

The subscript 'naught' or '0' refers to the current values of each density parameters. The subscripts R, M, k, and Λ refers to the fractional densities for radiation, matter, spatial curvature, and the cosmological constant. In standard cosmology, Equation 11 describes the mechanics of an expanding universe with current day densities.

1.2 Inflation

The ΛCDM model is a model that describes many observable features within our Universe. However, there are some features of the Universe that wasn't able to be explained like the horizon problem, the flatness problem, and the magnetic monopole problem. The theory of Inflation was created to deal with the incompatibilities. Inflation is a theory of an exponential expansion of space-time in the early Universe. This rapid and accelerated expansion is suspected to start at about 10^{-36}s after the Big Bang and ended at some time between 10^{-33}s and 10^{-32}s.[2] This time period will be referred to as the Inflationary Epoch. Inflation generated Primordial Gravitational Waves (PGWs). These PGWs distorted space-time and ultimately distorted any light that propagates through space-time. The affects of these PGWs could be observed from the B-mode polarization of the CMB but more on that in the next section. As far as our discussion of inflation, we will simply mathematically show Inflation and then explain the solutions to the horizon problem, the flatness problem, the magnetic monopole problem.

1.2.1 Inflationary Theory

As mentioned, Inflation is a rapidly accelerated expansion of space. To show this we will use Equation 3. From the ΛCDM model, the Universe is flat meaning the spatial curvature constant is 0. We need an exponential solution so ρ is a constant which corresponds to a cosmological constant dominated Universe. Then solving for $\dot{a}(t)$ we get the expression

$$\dot{a}(t) = a(t)\sqrt{\frac{8\pi G\rho}{3}} \tag{12}$$

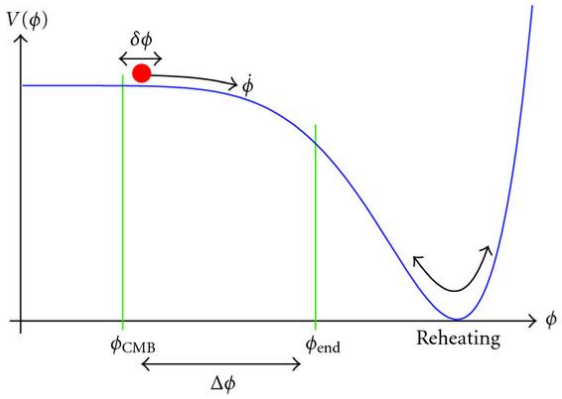

Figure 1: A depiction of SFSR model of Inflation.[10]

The solution of this differential equation is an exponential. The main thing to understand about Inflation is that you need the Universe to be dominated by something that resembles that cosmological constant because that is how you get exponential expansion. The cosmological constant means that there is some constant energy density per some unit volume and as you expand the density remains constant as seen in Equation 6.[2]

Single Field Slow Roll Model

In a simple inflationary model like Single Field Slow Roll (SFSR), you have a single scalar field, ϕ. You can write down the Hamiltonian for the system where there is two components: the kinetic energy and potential energy, V(ϕ). If the Hamiltonian is dominated by the kinetic energy then as space expands it won't act as a cosmological constant. This is because as space expands then the kinetic energy is going to redshift and the total energy would decrease. If the Hamiltonian is dominated by its potential energy, V(ϕ), then as space expands it would act as a cosmological constant. The potential energy is proportional to the value of the field and as space expands you have more space filled up with the same field. So, the energy density corresponds to the field value so as space expands the energy density is constant. This looks like a Universe dominated by the cosmological constant. That's where you get the "slow roll" because you want a model where the energy of the field is dominated by it potential energy and not its kinetic energy. You can see a depiction of this in Figure 1

You eventually want to roll down the potential energy hill because Inflation has to end. So the field must spend enough time in the state of high potential energy and low kinetic energy before it eventually trades that potential energy with kinetic energy. The field has to be nearly flat and eventually rolls to a minimum potential. Then at this point Inflation ends and Reheating begins which the process is out of the scope for this discussion. Now, that we have a simple understanding of Inflation, we will briefly discuss how Inflation solves the various problems that were not able to be explained by the ΛCDM model.[1]

1.2.2 Horizon Problem

From the Cosmological Principle the Universe is homogeneous and nearly isotropic which is the root of the horizon problem. Simply speaking, the horizon problem states that points at the different regions of the Universe should not have been in causal contact with each other due to the distances between them and the expansion of the Universe. The issue is that these points have the same temperature and other physical properties. However, these points shouldn't share these similarities since the transfer of information is limited to the speed of light. The ends of the Universe are too far away from one another for this transfer of information to occur and thus, for the Universe to have such uniformity in temperature. However, we do

observe that the Universe has these uniformity in temperature from the CMB so the Universe must have been thermal equilibrium at the time of Recombination. The concept of Inflation solves this problem by including a period of time where space-time rapidly expanded. From this brought seemingly disconnected regions together in causal contact before undergoing rapid acceleration. So, before Inflation these points were in causal contact but after rapid accelerated expansion they were not in causal contact.

1.2.3 Flatness Problem

As stated before the curvature of the Universe is defined by the mass density of space or the amount of mass-energy per volume. If there is a lot of matter or is positively curved then Density Parameter in Equation 10 is greater than 1 and the Universe is closed. If there is a small amount of matter or is negatively curved then Density Parameter is less than 1 and the Universe is closed. If there is enough matter to match Critical Density (Equation 9) then Density Parameter is approximately 1 and the Universe is flat. The Density Parameter that we currently measure is approximately 1 which means that the Universe is flat. The flatness problem is trying to understand why the Universe is flat. Observing that the Universe is currently flat implies that during the time of the early Universe it was even flatter. This mere observation begs the question of why is the Universe flat?

There is no reason to believe the the Universe started flat. We could assume that the Universe had some curvature at early times. Inflation solves this problem. Due to the exponential rapid expansion of space-time Inflation dilutes any curvature that the Universe could have had at early times. Meaning that the observable Universe is locally flat but the shape of the Universe could still be curved. The rapid expansion is necessary because if the expansion had happened more slowly, it would cause greater deviations from flatness or a larger deviation from the Density Parameter being 1.

1.2.4 Magnetic Monopole Problem

A magnetic monopole is a particle with a single magnetic pole. Magnetic monopoles can theoretically be created at extremely high temperatures. The ranges of temperature that were only present in the early Universe. During this time, magnetic monopoles should have been created in large amounts during the Big Bang and the early Universe. However, none have been observed. This is the Magnetic Monopole Problem.

There is no reason to believe that magnetic monopoles should not exist but they have not been observed. Inflation solves them problem. No matter how dense the magnetic monopoles could have been during Inflation the space in between the magnetic monopoles expanded so much that it left the monopoles spread out in space that we would never expect to see one. Meaning that the density of monopoles would have dropped exponentially and their abundance would drop to undetectable levels because they would exist in low densities. Inflation doesn't state that the magnetic monopoles can't or don't exist, it states that if they do exist we probably won't observe one.

1.3 Cosmic Microwave Background

At the time of the Big Bang, the Universe was in a very hot and dense state. In the early Universe random quantum fluctuations were present when inflation started and then were amplified to large scales during inflation. Space-time rapidly expanded from Inflation and resulting in the Universe cooling. This cooling allowed for clouds of dust and gas to collapse under gravity which resulted in the physical structures that we see today. But for the first 380,000 years, the Universe was filled with a hot plasma of free electrons and protons that light could not pass through. Photons would just be scattered off of these particles continuously. However, as the Universe cooled at a temperature of roughly 3,000K, these protons and electrons started to combine to form neutral Hydrogen, this epoch is known as Recombination. Neutral Hydrogen does not interact with light so at this point the Universe became transparent. The photons eventually scattered one last time and was able to continue freely through the Universe. This particular light from last scattering is know as the Cosmic Microwave Background (CMB). We can observe this radiation from the point of last scattering and it contains information regarding the state of the Universe at that time. The CMB is

almost completely uniform in temperature no matter which direction you look with minor deviations in the uniformity of temperature. The CMB is measured to have a temperature of $T = 2.72548 \pm 0.00057K$.[1] So, the CMB is completely uniform other than these minuscule fluctuations. In addition to the temperature fluctuations, there is a small amount of polarization in CMB which also contains information about the early Universe. This polarization will be the main topic of this section.

E-Mode and B-Mode Polarization

There are two sources of polarization in the CMB. The majority of the polarization in the CMB comes from density perturbations and the less frequent polarization comes from gravitational waves caused by Inflation. The crucial point is that E-modes are produced from these density perturbations where as the gravitational waves can produce both E-modes and B-modes. The E-mode patterns and B-mode patterns are produced by different physical mechanisms in the CMB.

If we think of the plasma in the early Universe, it was nearly uniform but there were small density fluctuations that would have produced different temperatures within the plasma. When the scattering light within that plasma was able to escape at the time of Recombination, they were near these temperature anisotropies thus getting polarized. This is the case because the light being emitted by the warmer part of the plasma will have a larger amplitude that the light being emitted by the cooler part of the plasma. This results in a net polarization in the direction of the warmer part of the plasma. Thus, this effect embedded E-mode polarization patterns in the CMB. Note, this polarization will only produce the Jacobian-like E-modes patterns in CMB.

As mentioned before there were random quantum fluctuations in space-time before Inflation began. During Inflation, the fluctuations would produce strong gravitational waves in the early Universe. As the Universe continued to evolve these gravitational waves would pass through the hot dense plasma and still be present during the time of the formation of the CMB. Gravitational waves are distortions in the curvature of space-time. If gravitational waves are propagating in a particular direction they will stretch and squeeze space in alternating directions. These distortions affect how light propagates through space-time causing redshifting and blueshifting. These gravitational waves will imprint specific patterns on the polarization of CMB known as E-Modes and B-modes. The E-mode polarization pattern and the B-mode polarization pattern is shown in Figure 2. The unique pattern to E-modes are a Jacobian-like structure whereas the unique pattern to B-modes are a curl-like structure. The reason, the BICEP program only looks for B-mode polarization is because the intensity of E-modes caused by density perturbations is greater than the E-modes caused by the gravitational waves.

In a general picture summery, the different models of Inflation makes predictions of the types of gravitational waves produced. The strength and properties of these gravitational waves determines the properties of the B-modes in the CMB. These B-modes are the signal in which the BICEP program aims to measure. These B-modes can help rule out or enforce different models of Inflation.

2 BICEP Program

The CMB is electromagnetic radiation that has been emitted from the Big Bang and is the oldest electromagnetic radiation in the Universe. When observed with a sensitive radio telescope, it is nearly isotropic. To explain the uniformity, the theory of inflation was developed smoothed out irregularities and to make sense of the observation of the CMB. From the rapid expansion of inflation produced Primordial Gravitational Waves (PGWs) that have too large of wavelengths to detect in current laboratories. However, the PGWs polarizes the light of the CMB in two different ways as mentioned above. The CMB is jumbled with polarizing lights from the foregrounds like dust. So, a device that is sensitive enough to not only detect the CMB but also separate the signal with other sources of polarizing light is necessary. The BICEP program was created to measure the polarization of the CMB and removing the noise from the foreground.

The BICEP program is a series of CMB experiments that aim to measure the polarization of the CMB with a focus on the curl component or B-mode polarization. There are a few iterations of telescopes that

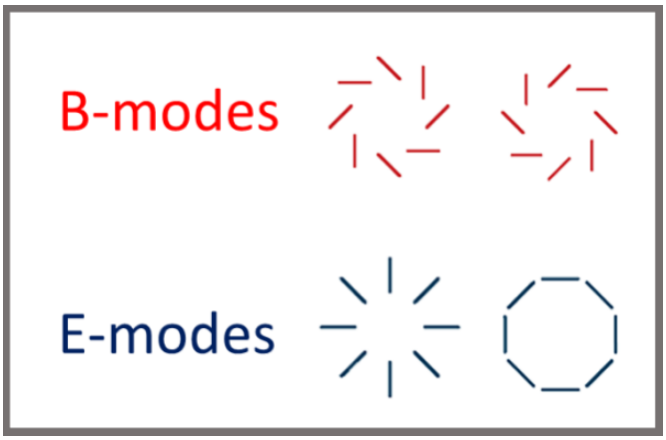

Figure 2: A depiction of B-modes and E-modes patterns. B-modes have a curl-like structure that rotate clockwise and counter-clockwise. E-modes have a Jacobian-like structure that extends outward or circles around a point. [11]

mainly consist of KECK Array, BICEP3 and BICEP Array. Each iteration has had similar design but upgraded with new detectors and different technology. The current iteration that is observing today is the BICEP Array. The BICEP program is located in Antarctica at the Amundsen-Scott South Pole Station with international collaborations from many Universities and Laboratories. The South Pole is a prime location for viewing the CMB because of the atmosphere and general position. Oxygen and water have absorption lines that are similar to the microwave spectrum. With extreme cold temperatures means reduced vapor and precipitation. Also, the South Pole is about 2800m about sea level meaning that there is even less atmosphere to sift through. However, one of the most important features about this location is that it is on the axis of rotation of the Earth. This means that you are able to view the same patch of sky, thus making it a prime location for observation. [6]

2.1 BICEP Program Background

The BICEP Program has operated since 2006, and consists of many stages of operation however, we will give attention to a few with the focus being on BICEP Array (BA). The BA detectors are an array of antennas attached to bolometers coupled with a Transition Edge Sensors (TES). The detectors collect the signal through the antennas and gets read out by the bolometer based of the change of resistance from the TES. The TES has a resistance change due to the heat received from the incoming light. So, the more of these bolometer-TES pairs the more sensitive the detectors are.

The KECK Array consisted of five receivers and are mounted together. KECK Array consisted of about 1,280 pairs of bolometers. The receivers observed B-mode polarization at the frequencies of 95Hz, 150GHz and 220GHz. The KECK Array allowed for a more detailed map of the CMB and the results were in agreement with results from previous BICEP operations.[3][4]

The next stage of operations was the deployment of BICEP3. BICEP3 was an upgrade of a previous telescope and was used in conjunction with the KECK Array. It had 1280 pairs of bolometers like the KECK Array and a 68cm aperture. BICEP3 started operations in 2015 and is currently still in operation. The receivers observed B-mode polarization at the frequencies of 95Hz, 150GHz, 220GHz and 270GHz. [3][4]

The most current stage of operation is replacing the KECK Array with four upgraded BICEP3-like telescopes all mounted together known as the BICEP Array. Until the construction and deployment of the other three upgraded BICEP3-like telescopes are completed, the empty slots in the mount are being used by three receivers from the KECK Array. When completed, the BICEP Array will have an estimated 15,000 pairs of bolometers and will observe over multiple frequencies at 30GHz-40GHz, 95 GHz, 150 GHz, 220 GHz

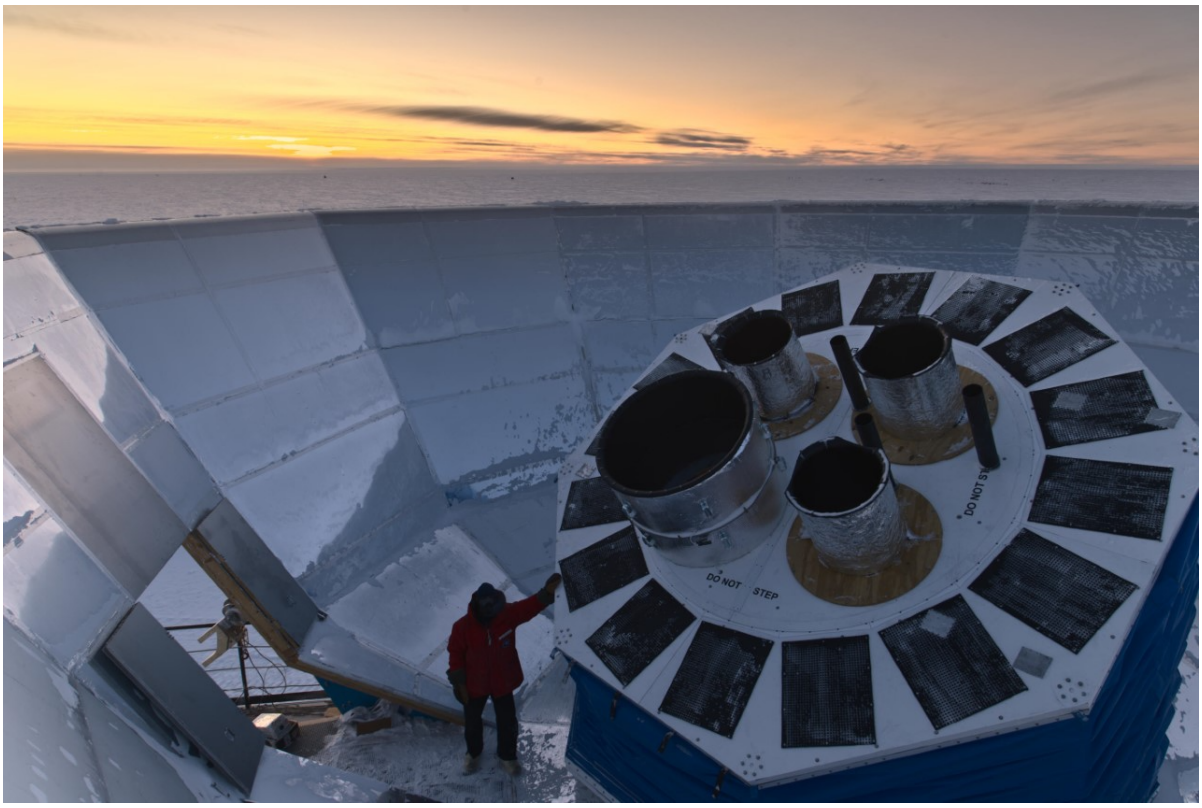

Figure 3: A photo of BICEP Array mount at South Pole. Photo taken by N Precup.

and 270 GHz. A current picture of the BICEP Array is shown in Figure 3.[3][4] The following analysis will solely be focused on the BICEP Array as it is the most current stage and the future of the BICEP Program.

2.2 BICEP Array Design

The BA is comprised of four BICEP3-like telescopes on a mount that is able to rotate about the bore-sight about the optical axis, the Azimuth and Elevation. The receivers observe in multiple bands of frequency. It is compact wide-field refracting telescope with a focal plane of arranged pairs of antenna-coupled polarization-sensitive transitions edge superconducting (TES) bolometers placed within a cryostat. The receivers use a Pulse Tube Cryocooler and a Helium Sorption fridge in order to cool the focal plane to the desired temperature of 280mK. These coolers are attached to the cryostat and focal plane by the use of flexible heat straps.

2.2.1 Cryostat

A cryostat is a device used to maintain low temperatures by different refrigeration techniques. The BICEP Array telescope consists of four cryostats surrounded by metal support systems. Each of the four cryostats are about 2.1m tall and 0.9m in diameter. In each cryostat there are three encased shells that are kept at different decreasing temperatures. The reason that the nested shells decrease in temperature from the outermost to the innermost shell until reaching the focal plane is to obtain and maintain the temperature of the focal plane. Since the CMB is 2.73K, the temperature that surrounds the focal plane must be considerably less than that. So the focal plane is kept in an environment of 280mK in the innermost shell. Inside the cryostat is kept under a vacuum. The shells are closed off with a window that is made from high-density

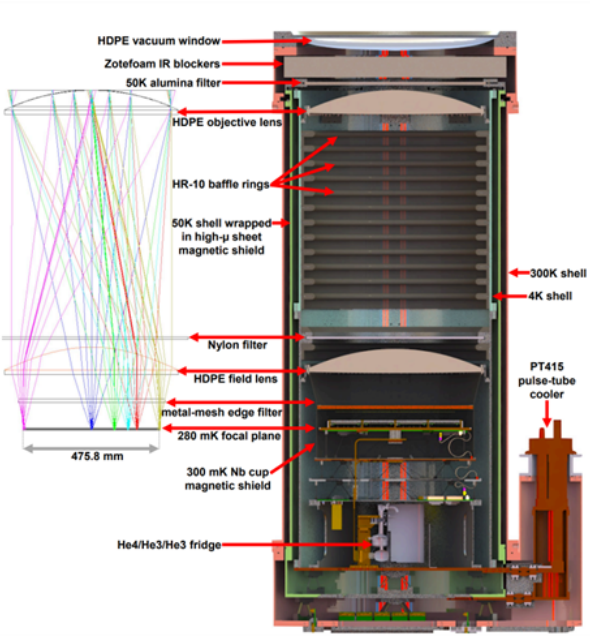

Figure 4: A cross-sectional view of the cryostat. The main focus of this figure is the cryostat itself. This image was gotten from Reference [4].

poly-ethylene (HDPE) as well as various infrared filters made from syrofoam, alumina and nylon. The window and filter allow light in, maintain a vacuum seal and to remove any radiation that is unwanted. All of the detectors and amplifiers are encased with a Niobium tank to shield them from magnetic fields that could possible pollute the signal. A cross-sectional visual of the cryostat can be seen in Figure 4.

The outermost shell is kept at a temperature of 300K and is in thermal contact with the environment. This shell contains the HDPE window and infrared filters. The next shell is kept at a temperature of 50K. The following shell is kept at 4K. The most notable contents of this shell are the HDPE objective lens, the HDPE field lens which is attached to the Niobium tank and the three-stage helium Sorption Fridge. Inside the Niobium tank is the focal plane which is kept at 280mK.

The 50k and 4k shells are cooled by the Pulse Tube Cryocooler which a closed loop helium cooler placed externally to the cryostat. The innermost area holds all of the focal plane with all of the receivers and amplifiers, the Sub-k stages and the three-stage Helium Sorption Fridge. The focal plane houses the detectors and amplifiers. The Sub-k stages or the "wedding cake" are carbon-fiber truss stages that goes through a series of cooling to 280mK that is thermally connected to the Helium Sorption by heat straps. It structurally supports the focal plane and is thermally connected to the Sorption Fridge and stainless steel blocks with heat straps. Between the focal plane are heat straps that connect to stainless steel blocks that act like a thermal filter to attenuate thermal noise from the control circuit. There are Temperature Control Modules (TCMs) on these steel blocks to measure, obtain and maintain the temperature on the focal plane. The Sub-k stages are located on a 4K base plate above the Sorption Fridge.

2.2.2 Housekeeping System

The Housekeeping (HS) in the BA has a couple of functions. Mainly, it reads out the temperatures from the various thermometers in the cryostat. The HS is located outside of the cryostat and contains three main components that consist of the HS: a data acquisition crate from United Electronics Industries (UEI Crate), the Backpack and the Receiver. Generally, the cryostat's thermometers collect the signal that gets sent through to the Backpack. The Backpack is external to the cryostat and contains daughter cards that

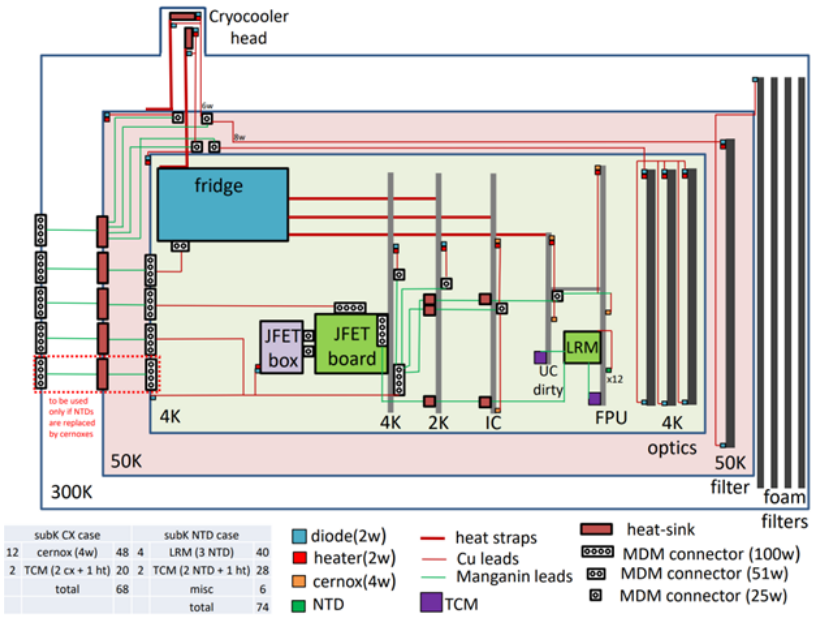

Figure 5: A schematic view of the BA cryostat; showing thermometry and thermistor layout. This schematic shows the same thing as Figure 4 but not scaled the same. The purpose of this figure is to give you a visual representation of where the diodes, Cernox, NTDs and TCMs are installed at. The gray lines labeled "4K", "2K", "IC" and "FPU" are layers of the "wedding cake". [5]

that reads out the different thermometers and thermistors within the cryostat. Then the signal gets sent to the UEI crate where the signal then gets digitized. This digitized signal gets sent to the General Control Program (GCP); a software that reads out and saved the data collected.

There are four types of thermometers and thermistors that are used in the cryostat that get readout from the HS. These thermometers and thermistors are the main focus of this paper as they were the main analysis. There is the DT-670 Silicon Diode from LakeShore [9] that are located in the 50K and 4K shells in the cryostat. However, this diode has an operation range from 1.4K to 500K which is why this is an ideal electronic for the higher temperature stages in the cryostat.[6] Then there is the Cernox Thermistors from LakeShore [9] and the Allen-Bradley Carbon Thermistor in the cryostat. They have the same readout circuitry but just differ by reading out different parts of the cryostat. They have an operating range of 100mK to 400K with higher sensitivity at lower temperatures.[6] So they are mainly used in the 4K stage and the sub-K stage stage. Lastly, there is the Neutron Transmutation Doped (NTD) Germanium Thermistor that are used in the sub-K stages specifically with the Temperature Control Module (TCM) and the focal plane. A view of the cross-section of the cryostat with the thermometer and thermistor placements can be seen in Figure 5.

The signal from the thermometers and thermistors get sent to the Backpack that holds the daughter cards. There are 36 daughter cards which processes the analog signal from the sensors in the cryostat. These daughter cards are used for biasing and reading out the thermometers and thermistors contained within the cryostat. The sends this signal to the UEI crate to digitize the signal.

In order to get the cryostat to operate properly a lot of these different elements that need to be calibrated. In particular, the daughter cards responsible for reading out diode and Cernox thermometer. Which brings us to two of the main topic of this thesis which is to ensure that the diode daughter cards and Cernox daughter cards are properly calibrated.

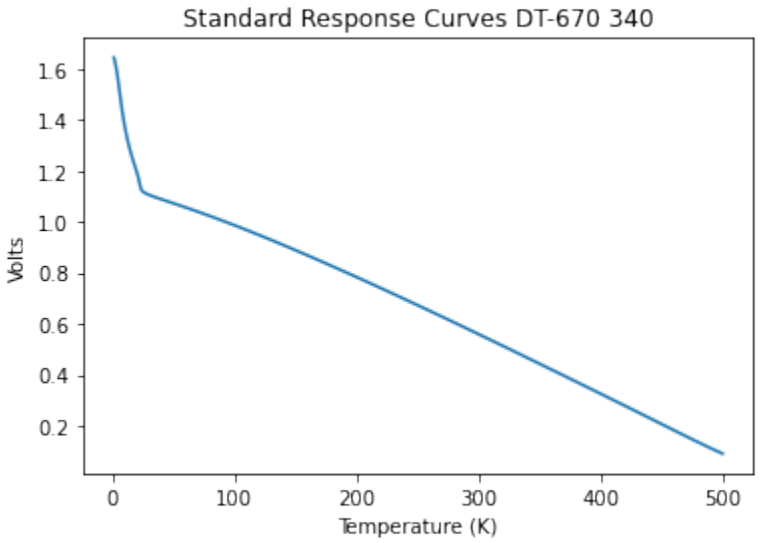

Figure 6: Lakeshore DT-670 Diode's Standard response Curve

3 Silicon Diodes Thermometer

3.1 The Circuit

The circuit works by putting a 10 μA current bias through the diode which will produce some voltage across the diode, it then it ideally amplifies that voltage by a factor of four. The input voltage is the voltage that is ran through the diode. Whereas the output voltage is the measured voltage by the UEI crate that gets amplified after running through the circuit. The difference between the input voltage and the output voltage should be a gain of four. The circuit is designed to have a gain of four and we want to measure what it actually is. We have to calibrate the gain and the offset of the circuit because they could vary. We want to know them precisely. Now the from the standard curve (Shown in Figure 6) given from LakeShore we have a calibration function represented as

$$T = f(V_{in}) \tag{13}$$

The Lakeshore DT-670 Diode's calibration curve is the voltage that you should obtain when you run 10 μA of current through the diode at a given temperature. This is why the circuitry within the daughter cards runs a 10 μA current bias through the diode. Notice that there is two relatively different behaviors in the standard response curve. From the low temperatures of about 1.4K to 30K the response curve is much steeper than the response curve from 30K to 500K. This is a displays the fact that the diode is more sensitive at these lower temperature ranges than the higher temperature ranges.

3.2 Calibration

The main purpose of this chapter is to discuss the testing and calibration analysis of the diode daughter cards that will be used to bias and read the Lakeshore DT-670 Diode thermometers. We partially constructed the HS by building the motherboard to test the diode daughter cards. We connected this HS to UEI crate which connects to the GCP and a standard bench voltage power supply to supply power to the motherboard. There were six daughter cards with the diode thermometers each of which is labeled with a serial number (8, 17, 19, 20, 21, 22). We inserted each daughter card into one of the "slots" on the motherboard which reads out the different thermometers and controls the different types of heaters. Each "slot" is correlated to the different channels that are associated with the cryostat. These "slots" are labeled "J12" and "J13". The

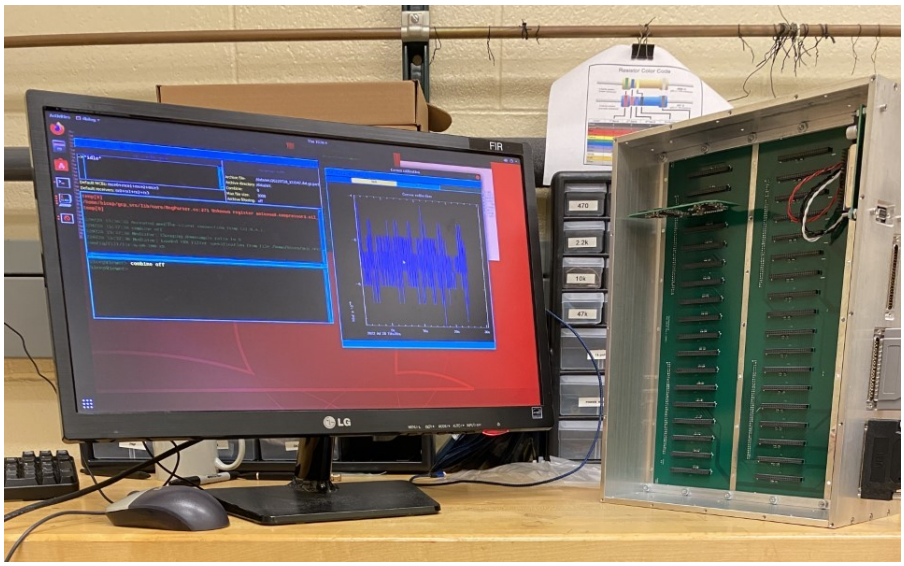

Figure 7: A picture of the general set-up. The computer screen on the left of the photo shows the GCP. The silver box with the motherboard is the Backpack. Inside the backpack you can see the motherboard with a daughter card inserted into a slot. Each of the black spaces on the motherboard are the "slots" referred to above.

channels are the different components that are being monitored by the HS within the cryostat. The diode daughter card contains four circuits that can operate the readout of four diodes in one "slot". We tested the first two circuits on each daughter card on two "slots" i.e. "J12" and "J13". Each circuit is associated to a specific channel that is responsible for a diode readout. Channels A and B were associated with slot "J13". Channels C and D were associated with slot "J12". We measured the output voltage from the first two circuits of each of the six daughter cards over fifteen different resistors on two different "slots". The resistors were placed across the diode daughter card input to imitate the diode thermometer. Each test of the output voltage on the resistor took approximately five minutes. Over this five minute period of time, the UEI crate is registering the voltage outputs of this circuit on a distinct channel that would monitor a particular component on a fully constructed cryostat. It is then being displayed by the GCP. The GCP calculates the mean of the voltage outputs in real time as well. A display of the setup can be seen in Figure 7 and Figure 8. The goal of this experiment is to calculate the uncertainty in the offset voltage of the circuit, the gain of the circuit and the temperature measurements in the Housekeeping System.

3.2.1 Calculating the Uncertainties in the Output Voltage

Since there is a large amount of data, I will demonstrate a calculation for one diode daughter card on a single channel while explaining the analysis. Once the measurements of the resistors and the mean output voltage was collected we simply plotted the data for the diode daughter card as Mean Voltage vs Resistance. Then you'd be able to see that the diode daughter card has a linear dependence on the resistance applied to the mean voltage output. We can then use a linear model to fit this data as shown in Figure 9. The general linear model is written as

$$V_{out} = \alpha R + \beta \tag{14}$$

Figure 8: A picture of the UEI crate that connects the backpack to the GCP.

where,

$$\begin{aligned} V_{out} &= measured\ output\ voltage \\ \alpha &= estimated\ measure\ of\ the\ bias\ current\ and\ circuit\ gain \\ R &= measured\ resistance \\ \beta &= estimated\ offset\ voltage \end{aligned}$$

Now α is a product of the bias current (10 μA) and the gain (expected to be 4) so we should ideally measure α to be 40 μA. β is the voltage offset so ideally we should measure it to be 0V.

Next, we will perform a Chi-Squared Test. The Chi-Square is normally used to test and compare two different types of data: observed data and expected data. It measures what is called the "goodness to fit" which is the difference between what you'd expect and what has been observed. However, we want to use the Chi-Square test to obtain the uncertainties on the output voltage measurements. We are going to assume "goodness of fit" to derive these uncertainties. We are using the fluctuations of the data around the model to estimate the error on the data. The Chi-Square Test is generically given by

$$\chi^2 = \sum \frac{(Observation - Model)^2}{Error^2} \tag{15}$$

Where,

$$\begin{aligned} Observation\ is\ the\ data\ collected\ from\ our\ tests. \\ Model\ is\ estimated\ values\ that\ we\ used\ to\ fit\ our\ data. \\ Error\ is\ the\ uncertainty\ of\ the\ data\ collected. \end{aligned}$$

The Chi-Square Test for our diode is

$$\chi^2 = \sum \frac{(V_i - \alpha R_i - \beta)^2}{\sigma_V^2} \tag{16}$$

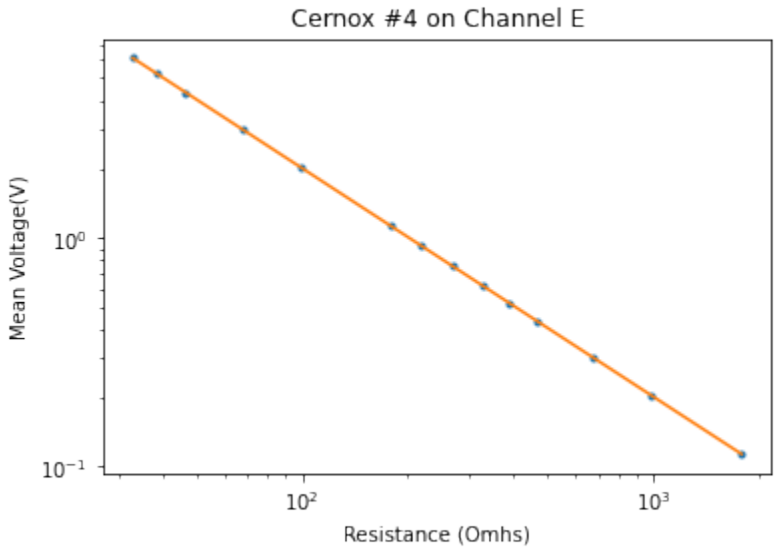

Figure 9: Data and model fit for Diode 08 on Channel A. Visually, the model fits well. Also, the results are expected; the mean voltage output increases with resistance.

Where,

$$\begin{aligned} V_i &= \textit{mean output voltage measured for each resistor.} \\ R_i &= \textit{the measured resistance for each resistor.} \\ \sigma_V &= \textit{the uncertainty of the output voltage.} \end{aligned}$$

We have found the best fit parameters, α and β, by minimizing χ^2 and fitting our data to our general linear model in Equation 14 for verification of the fit. For this specific diode, our calculated best fit parameters are

$$\alpha = .00004032A \tag{17}$$

$$\beta = -.002243V \tag{18}$$

All of the other α and β values can be found in Appendix 1 and 2. With out best fit parameter, we want to estimate the uncertainty in the output voltage by assuming that the minimum value of χ^2. To do that we set χ^2 equal the number of data points (degrees of freedom) minus the number of fit parameters. Degrees of freedom are the measurements of the number of values in the statistic that are free to vary without influencing the result of the statistic. In this case, the degrees of freedom is the number of resistors tested which is fifteen resistors so the minimum χ^2 is

$$\chi^2_{min} = \sum \frac{(V_i - \alpha R_i - \beta)^2}{\sigma_V^2} = 13 \tag{19}$$

Thus, the uncertainty in the output voltage measurement is

$$\sigma_V = \sqrt{\sum \frac{(V_i - \alpha R_i - \beta)^2}{13}} \tag{20}$$

The uncertainty for our example is approximately

$$\sigma_V = \sqrt{\sum \frac{(V_i - .00004032 * R_i - .002243)^2}{13}} = .001630V \tag{21}$$

3.2.2 Calculating the Uncertainties on α and β

The goal of this project is to test calibration of these daughter cards to ensure proper temperature measurements of the cryostat. We need to propagate the error estimates on the voltages shown above to calculate the uncertainty in α and β. Then we can use that to get the uncertainties on the temperature measurements of these diodes. We use the Hessian and then the Fisher Information to accomplish this.

But first, to find the uncertainty on α and β we can use the Hessian Matrix or the Hessian for short. We write the Hessian as a square matrix of second-order partial derivatives of χ^2 with respects to our parameters. It describes the local curvature of a multi-variable function. In this case it describes the curvature of our parameters α and β meaning that the Hessian will describe the impact of altering α and β to our model fit. We write the Hessian as

$$H = \begin{bmatrix} \frac{\partial^2 \chi^2}{\partial \alpha^2} & \frac{\partial^2 \chi^2}{\partial \alpha \partial \beta} \\ \frac{\partial^2 \chi^2}{\partial \alpha \partial \beta} & \frac{\partial^2 \chi^2}{\partial \beta^2} \end{bmatrix} \tag{22}$$

Performing the calculations for the diode results in

$$H = 2 \begin{bmatrix} \sum \frac{R_i^2}{\sigma_V^2} & \sum \frac{R_i}{\sigma_V^2} \\ \sum \frac{R_i}{\sigma_V^2} & \frac{N}{\sigma_V^2} \end{bmatrix} \tag{23}$$

To know the uncertainty of our gain (α) and voltage offset (β) we simply just need to calculate the inverse of the Hessian shown below.

$$\sigma_\mu^2 = H^{-1} \tag{24}$$

$$\sigma_\mu^2 = \frac{1}{2} \frac{1}{(\sum \frac{R_i^2}{\sigma_V^2})(\frac{N}{\sigma_V^2}) - (\sum \frac{R_i}{\sigma_V^2})^2} \begin{bmatrix} \frac{N}{\sigma_V^2} & -\sum \frac{R_i}{\sigma_V^2} \\ -\sum \frac{R_i}{\sigma_V^2} & \sum \frac{R_i^2}{\sigma_V^2} \end{bmatrix} \tag{25}$$

The uncertainty on $\bar{\alpha}$ is the first diagonal entry of the inverse Hessian.

$$\sigma_\alpha^2 = \frac{1}{2} \frac{1}{(\sum \frac{R_i^2}{\sigma_V^2})(\frac{N}{\sigma_V^2}) - (\sum \frac{R_i}{\sigma_V^2})^2} (\frac{N}{\sigma_V^2}) \tag{26}$$

The calculated results for our example diode is

$$\sigma_\alpha = 5.400 * 10^{-9} A \tag{27}$$

The uncertainty on β is the second diagonal entry of the inverse Hessian.

$$\sigma_\beta^2 = \frac{1}{2} \frac{1}{(\sum \frac{R_i^2}{\sigma_V^2})(\frac{N}{\sigma_V^2}) - (\sum \frac{R_i}{\sigma_V^2})^2} (\sum \frac{R_i^2}{\sigma_V^2}) \tag{28}$$

The calculated results for our example diode is

$$\sigma_\beta = 3.763 * 10^{-4} V \tag{29}$$

All of the other σ_α and σ_β values can be found in Appendix 3 and 4.

3.2.3 Calculating the Uncertainties on the Temperature Measurement

Recapping on what we have accomplished so far into what we hope to accomplish. First, we assumed best fit for χ^2 to estimate the errors on the measured voltage outputs associated with individual resistors for each of the diode daughter cards. Then we propagated those errors to calculate the errors associated with the gain (α) and offset voltage (β) by calculating the inverse Hessian matrix. Lastly, we want to calculate the errors on the temperature measurement for each diode thermometer assuming the standard response curve (Figure 6) of the diodes. We accomplish this by computing the Fisher Information.

The Fisher information is a way of quantifying the amount of information an observation carries about a parameter. Generally, it provides the framework for reasoning about a parameter uncertainty. We can generally write the Fisher Information as

$$F_T = \frac{\partial \mu^T}{\partial T} H \frac{\partial \mu}{\partial T} \tag{30}$$

where,

$$\frac{\partial T}{\partial \mu} = \textit{ the Jacobian}$$
$$\frac{\partial T^T}{\partial \mu} = \textit{ the transpose of the Jacobian}$$
$$H = \textit{ the Hessian}$$

The uncertainty on the temperature squared is the inverse of the Fisher Information as shown

$$\sigma^2_{Temp} = F_T^{-1} \tag{31}$$

In order to calculate the Fisher Information, we need to calculate the Jacobian. Writing the Jacobian for the parameters of the model (α and β) and the general expression for temperature in Equation 13 from the calibration curve results in

$$J = \begin{bmatrix} \frac{\partial T}{\partial \alpha} \\ \frac{\partial T}{\partial \beta} \end{bmatrix} \tag{32}$$

First, we need to recognize that the temperature function in Equation 13 is a function of the input voltage so we must rewrite Equation 14 to be in terms of the input voltage.

$$V_{in} = \frac{I_{bias}(V_{out} - \beta)}{\alpha} \tag{33}$$

Next, need to use of the chain rule so we then can find how the temperature changes with each parameter, μ.

$$\frac{\partial T}{\partial \mu} = \frac{\partial T}{\partial V_{in}} \frac{\partial V_{in}}{\partial \mu} \tag{34}$$

Solving the partial derivative for each parameter allows us to write the Jacobian for the diode.

$$J = -\frac{\partial T}{\partial V_{in}} \frac{1}{\alpha} \begin{bmatrix} \frac{(V_{out} - \beta)}{\alpha} \\ I_{bias} \end{bmatrix} \tag{35}$$

Substituting, Equation 14 for V_{out} so our Jacobian is completely in terms of V_{in} results in

$$J = -\frac{\partial T}{\partial V_{in}} \frac{1}{\alpha} \begin{bmatrix} V_{in} \\ I_{bias} \end{bmatrix} \tag{36}$$

This shows us how the temperature changes when each of the parameters, α and β, are altered. Notice that both rates of change depend on the slope of the standard response curve of the diode and the gain of the

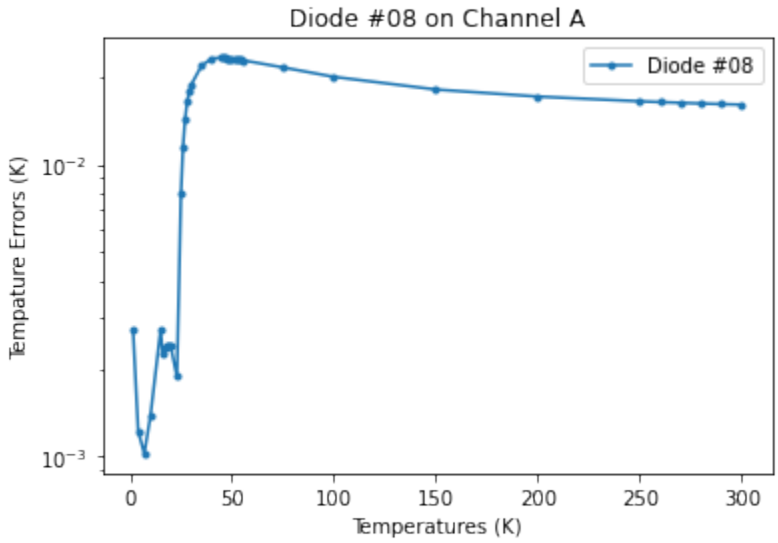

Figure 10: Temperature Uncertainty for Diode 08 from the Temperature ranges of 1.4K to 300K. As mentioned before, the most critical measurements are around 4K and 50K. From this figure, that want the 4K temperature uncertainty to be in the range of mK. Below about 40K is within the mk range whereas above 40K is in tens to hundreds of mK range.

diode circuit. Also, note that the Jacobian for α depends on the input voltage where as the Jacobian for β is constant with the bias current.

With the Jacobian (Equation 36) and the Hessian (Equation 23) for the diode, we can now calculate the Fisher Information demonstrated below.

$$F_T = \frac{\alpha^2}{(\frac{\partial T}{\partial V_{in}})^2} \begin{bmatrix} V_{in}^{-1} & I_{bias}^{-1} \end{bmatrix} \begin{bmatrix} \sum \frac{R_i^2}{\sigma_V^2} & \sum \frac{R_i}{\sigma_V^2} \\ \sum \frac{R_i}{\sigma_V^2} & \frac{N}{\sigma_V^2} \end{bmatrix} \begin{bmatrix} V_{in}^{-1} \\ I_{bias}^{-1} \end{bmatrix} \tag{37}$$

$$F_T = (\frac{2}{\sigma_V^2})(\frac{\alpha^2}{(\frac{\partial T}{\partial V_{in}})^2})(\sum \frac{R_i^2}{V_{in}^2} + 2\sum \frac{R_i}{V_{in} I_{bias}} + \frac{N}{I_{bias}^2}) \tag{38}$$

Where N is the number of data points. To solve for the uncertainty in temperature, σ_{Temp}, we simply rewrite Equation 31 and substitute in the calculated Fisher Information to obtain

$$\sigma_{Temp} = \frac{1}{\sqrt{F_T}} \tag{39}$$

We can now calculate the uncertainty in the temperature measurements of a diode thermometers as a function of temperature. For this particular diode, we calculated the uncertainty for the range of temperatures 1.4K to 300K shown in Figure 10. We chose this temperature range because this is the operating range for the diodes in the cryostat.

3.2.4 How Well Do We Need to Know the Calibration?

D. Goldfinger is testing the 50K heat strap which goes from the pulse tube to the 50K cylinder with his results stated in Figures 11 and **??**. There is a temperature difference across that strap. The colder temperature (indicated by the orange data in Figure 11) is on the pulse tube is on the telescope side of the strap. There is a relatively big temperature difference across that strap. There is heat hitting the 50K stage, primarily through the incoming infrared emissions which results in a certain amount of power (W). D. Goldfinger

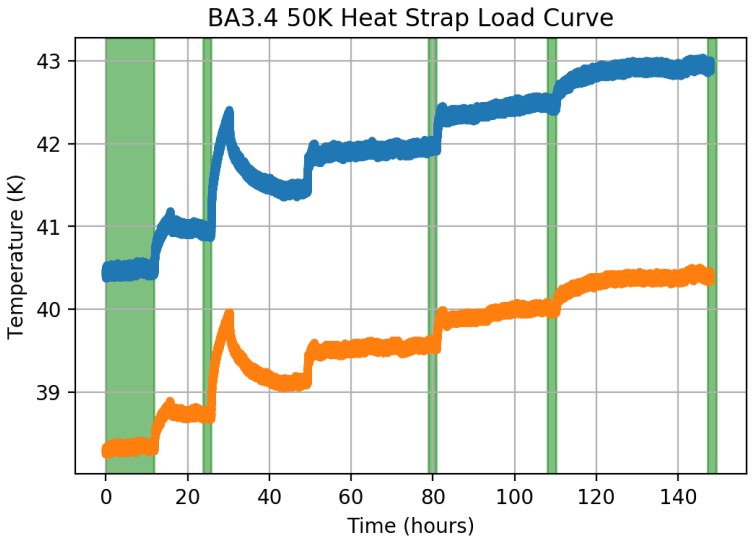

Figure 11: Heat load measurement for BA3.4 50K Heat Strap.[8]

estimates the load at 62.6 ± 3.8W.[8] If there is this amount of power on this isolated strap, will cause the strap to heat up. However, it is prevented from heating from the pulse tube. All of the heat that is getting pumped out of the system is transferred through the heat strap which is acting like a resistor. There is a certain amount of thermal current in units of power (W). Because of the thermal resistance of the heat strap it's going to cause a temperature difference across the strap. That temperature difference is roughly 2K at time 0. You can see that the temperature steps up in time. He is adding heat the side of the heat strap that's attach to the 50K shell. If you are adding heat, you are adding to the load making a larger temperature difference. At time 0, we are not generating any power on the resistor but there is still a temperature difference across the strap. This temperature difference tells us the normal the amount of load on this 50K stage. This relies entirely on comparing these two thermometers. By shifting these temperature measurements results in an inaccurate loading measurement. He estimates about a 6% on the loading estimate. This means that we don't want our calibration error to exceed 6% of this difference with an additional factor of $\frac{1}{\sqrt{2}}$ due to having two thermometers. So, we don't want our calibration error to exceed about 85mK to ensure the success of these types of measurements at 50K. Quickly quoting the results for the 4K heat strap, we don't want our calibration error to exceed 10mk.

We hope the error on the temperature measurement for these diode daughter cards to be in the range of a few mK. We can see that the error below 40K in Figure 10 are within this range but the error above 40K is within the range of calibration error, which is a good sign.

3.3 Results

As stated above we did this analysis for six different diode daughter cards on two different "slots" and tested only the first two circuits on the diode daughter card. We will now analyze data comparing a single diode daughter card on each different channel. Then we will compare all the diode daughter cards on a single channel. First, we will examine a single diode daughter card on each different channel and we will continue our example above shown in Figure 13.

Now we don't have a reason to believe that the temperature uncertainty on one channel should be substantially larger than another or the temperature uncertainty for one diode daughter card should be substantially larger that another. All channels measured are within our temperature error estimate given above. In Figure 12, Channel D has errors that are 10 times larger than Channel A. We calculate the fit for

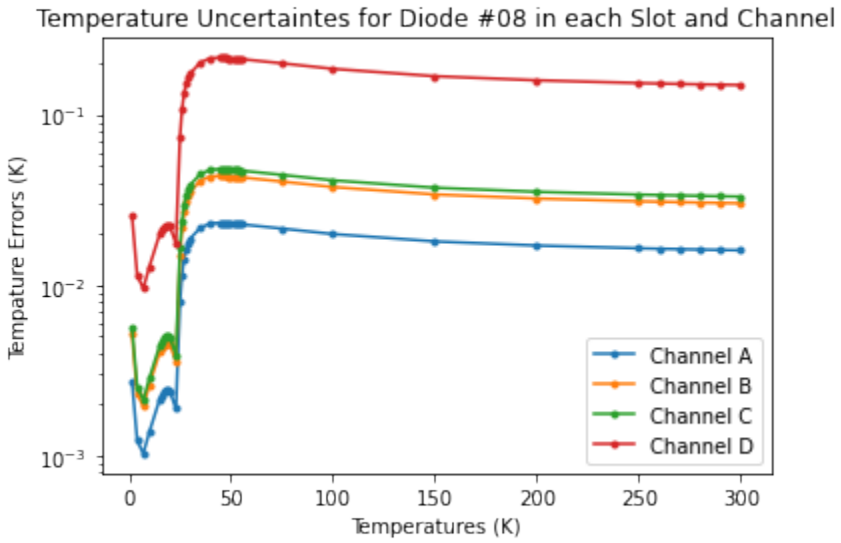

Figure 12: Temperature Uncertainties for each channel on Diode Daughter Card 8. This shows a cause for concern because it seems that there is a difference in measurement from channel to channel. On Channel D, even the values below 40K are in the range of tens of mK and the range above 40K is hundreds mk to a K.

Channel A and Channel D to by using Equation 14 and finding the best fit parameters for each channel. We can then find the difference between the observed data and the model fitting of this data to compute the deviations for each channel shown as

$$\Delta V = V_i - \alpha R_i - \beta \tag{40}$$

We do this to see if there are outlying data points that are causing the temperature uncertainty to be an order of magnitude difference from each other on Channel A and Channel D. So, we can plot these deviations against our resistance values to view the scatter of each channel which is represented in Figure 13.

Figure 13 demonstrates a cause for concern. It shows that the deviations from our measured voltage data and model are substantially larger on one channel than another which could go against what we would believe and without a clear reason why this is the case. But before we make this conclusion, let's take a deeper dive. In Figure 14, I show the computational results of each separate diode daughter card for all of the channels tested. This raises an even larger level of concern as it shows that these deviations are not unique to one specific diode.

We will then use the calculated deviations from Equation 40 to reorganize our data to compare the performance of a singular diode daughter card on each channel shown in Figure 15; again, to see if it may be an outlying data point.

Upon investigation, it looks like that we were wrong in the assumption that the temperature uncertainty on one channel should not be substantially larger than another. We can see that the temperature uncertainty on the diode thermometer most definitely depends on the channel in which it is inputted in.

Let's look at the same data in a different light. Let's now use the same computations for temperature uncertainty comparing each diode to a single channel which is shown in Figure 16.

Reviewing these graphs you can see that even the diodes have a notable difference in temperature uncertainty from one another on a single channel. Using Equation 40 to calculate the deviations of each diode is shown in Figure 17.

Something interesting can be evaluated from Figure 17. The deviations are different for each channel. In Figure 17a and Figure 17c the deviations for the diodes are on the order of mV whereas in Figure 17b and Figure 17c the deviations for the diodes are on the order of tens of mV. This give reason to believe that some

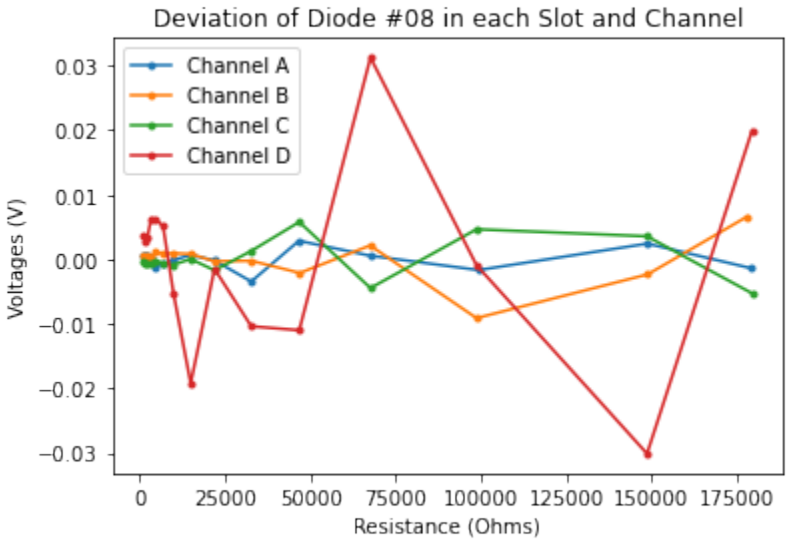

Figure 13: Deviation Comparison of data from model. Here we can see that the deviations are large on Channel D which causes the overall uncertainty measurement of temperature to be substantially larger than the other channels.

channels have more reliable readouts than others. Which means that the calibration of the diode daughter cards are a must and require more attention to ensure that the temperature in the cryostat is properly maintained. However, the good news is that the majority of the uncertainty measurement lie within the the calculated uncertainty range.

One outcome of this, is that if certain channels on certain daughter cards are going to have a higher level of noise then we can give ways to improve this experiment for the future. If the BICEP Program is worried about these high noise levels and want to bring the uncertainty down, simply taking more data points by testing more resistors on each daughter card would reduce the uncertainty. In Equation 38, has a dependence on the amount of resistors used in the calculation so the more resistors you use to imitate the diode the greater the Fischer Information.

4 Cernox Thermistor

In this chapter we will discuss the testing and calibration analysis of the Cernox daughter cards that will be used to bias and read the LakeShore Cernox 1010 thermistor. The process of testing the Cernox daughter cards are exactly the same as the testing for the diode daughter cards as mentioned above. However, the key differences is that the Cernox daughter cards only have two circuits on the board instead of four; the circuitry is different. The parameters are different units. The range of resistances are a bit different. Also, the Cernox daughter cards were plugged into slots "J5" and "J6". Channels E and F corresponds to slot "J5" and Channel G corresponds to slot "J6". There were ten daughter cards with Cernox thermistors with different serial numbers (4, 5, 6, 7, 9, 10, 11, 25, 34, and 35). We measured the voltage output of each of the ten daughter cards over fourteen different resistors on three different channels. Again, the goal of this experiment is to calculate the uncertainty in the offset voltage of the circuit, the gain of the circuit and the temperature measurements in the Housekeeping System.

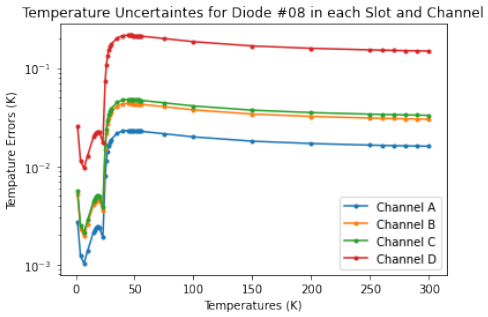

(a) Channel's Temperature Uncertainties for Diode 8

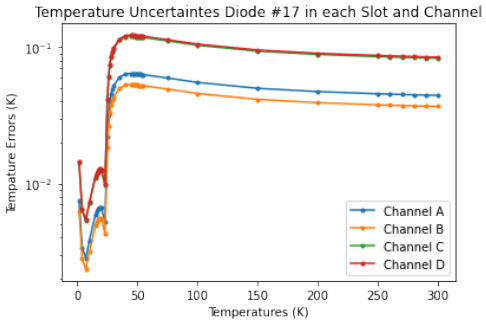

(b) Channel's Temperature Uncertainties for Diode 17

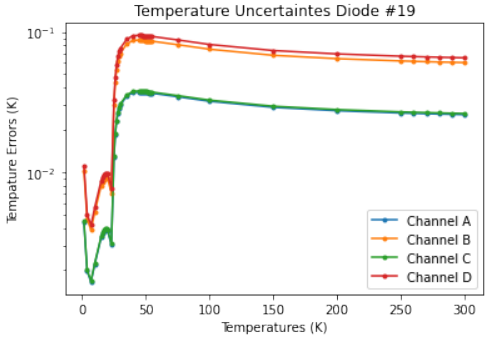

(c) Channel's Temperature Uncertainties for Diode 19

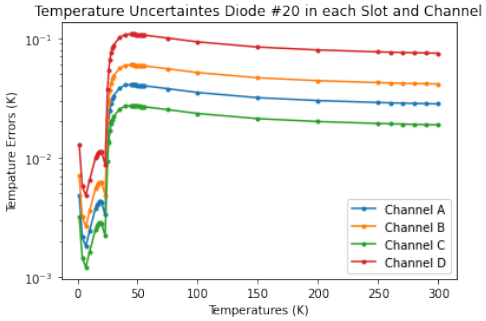

(d) Channel's Temperature Uncertainties for Diode 20

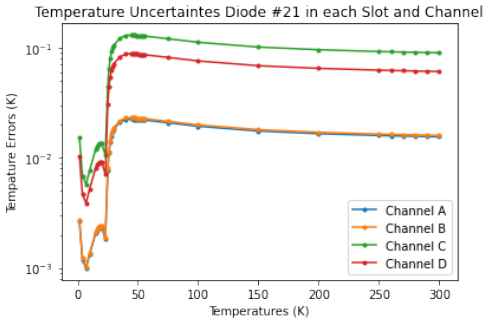

(e) Channel's Temperature Uncertainties for Diode 21

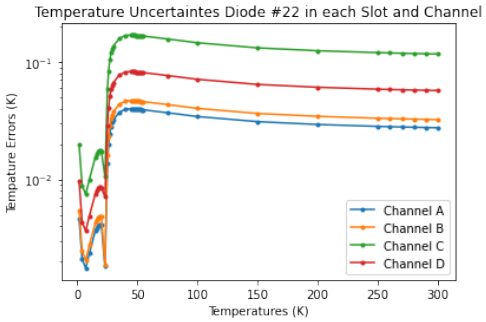

(f) Channel's Temperature Uncertainties for Diode 22

Figure 14: Each Channel's Temperature Uncertainties for each Diode

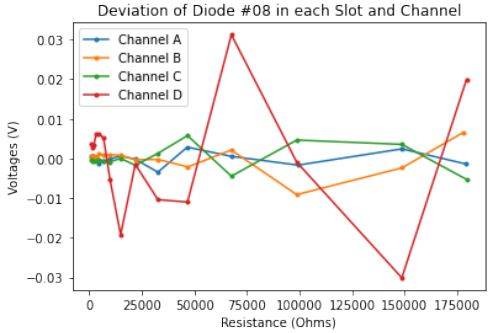

(a) Channel's Deviations for Diode 8

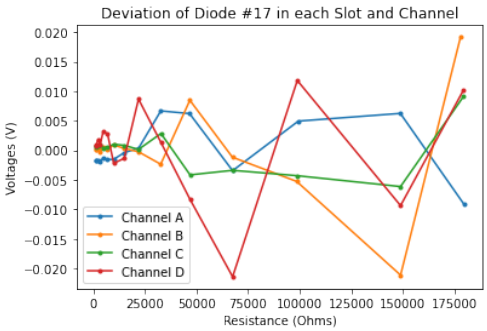

(b) Channel's Deviations for Diode 17

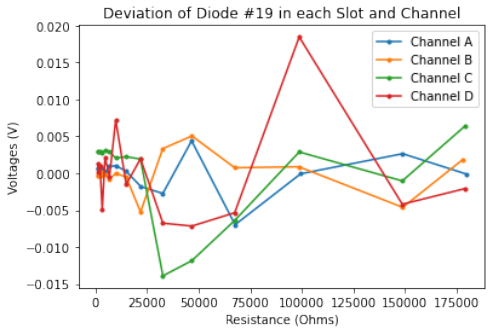

(c) Channel's Deviations for Diode 19

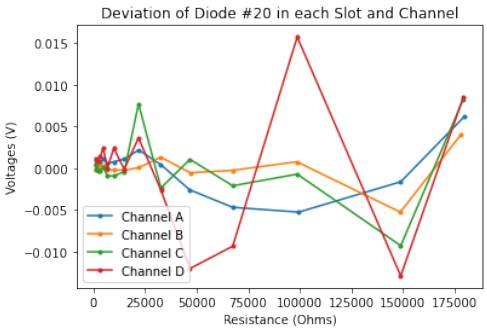

(d) Channel's Deviations for Diode 20

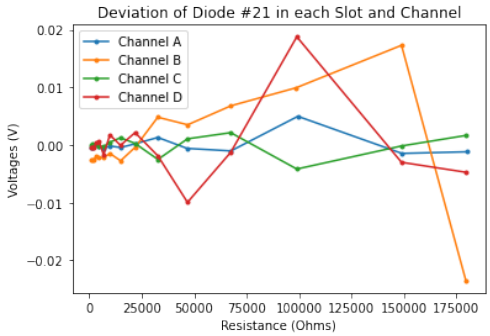

(e) Channel's Deviations for Diode 21

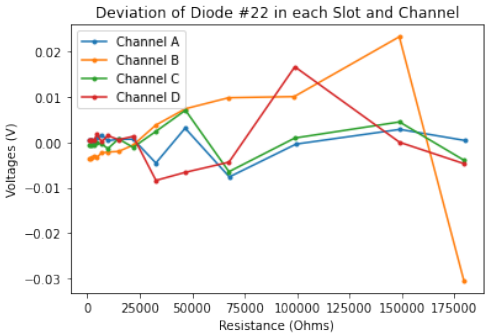

(f) Channel's Deviations for Diode 22

Figure 15: Each Channel's Deviations0 for each Diode

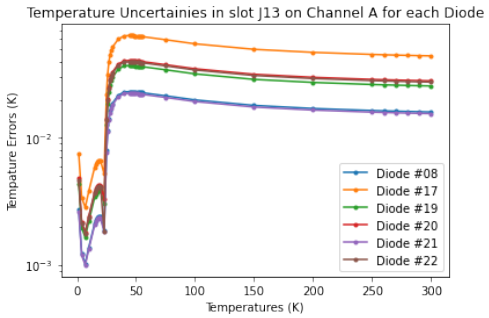

(a) Diode's Temperature Uncertainties on Channel A

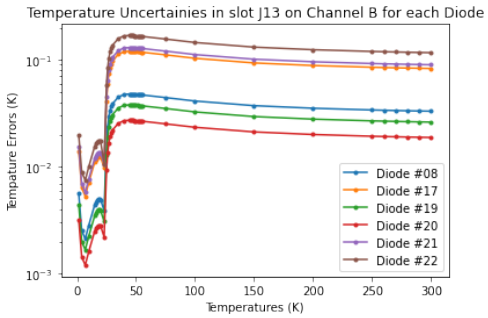

(b) Diode's Temperature Uncertainties on Channel B

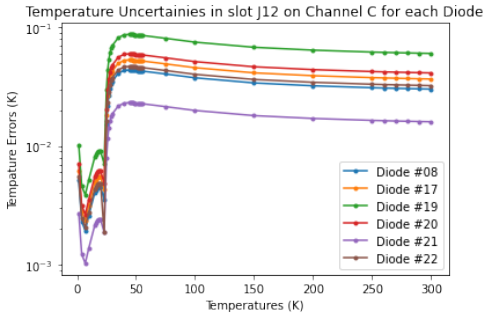

(c) Diode's Temperature Uncertainties on Channel C

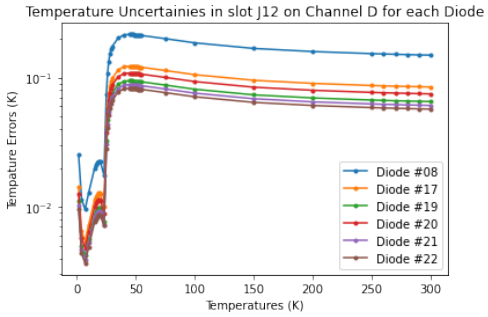

(d) Diode's Temperature Uncertainties on Channel D

Figure 16: Each Diode's Temperature Uncertainties on each Channel

4.1 The Circuit

The Cernox circuit provides a feedback loop in such a way that produces a 50μV AC voltage through the Cernox thermistor. We measure the current through a sense resistor. The Cernox daughter card is a 4-wire measurement. The Cernox has an unknown resistance and it applies a current bias through this resistor which uses a set of wires to measure this resistor. Then the circuit uses a feedback look to adjust the current bias in order to achieve a target voltage, 50μV, across the Cernox and then it senses the current required to achieve that voltage with a sense resistor. Then this current is sent through some active low pass filters and amplifies the output voltage that is digitized by UEI crate. Now the from the standard curve (Shown in Figure 18) given from LakeShore we have a calibration function represented as

$$T = f(R) \tag{41}$$

The Lakeshore 1010 Cernox calibration curve shows the resistance as fuction of temperature. This is why the circuitry within the daughter cards runs a 50 μV current bias through the Cernox. Notice that there is two relatively different behaviors in the standard response curve. From the low temperatures the response curve is extremely steeper than the response curve from higher temperatures. This is a displays the fact that the diode is more sensitive at these lower temperature ranges than the higher temperature ranges. This demonstrates behavior that we would expect from a thermistor.

4.2 Calibration

4.2.1 Calculating the Uncertainties on the Output Voltage

Since there is a large amount of data, I will demonstrate a calculation for one Cernox daughter card on a single channel while explaining the analysis. The analysis of the Cernox daughter card is similar to the diode

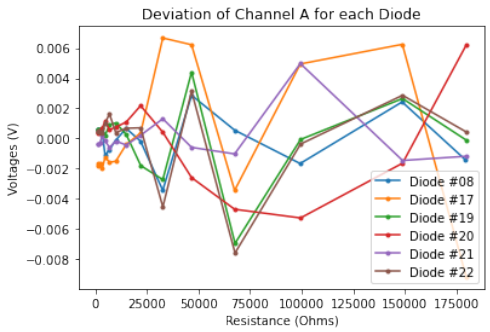

(a) Diode's Deviations on Channel A

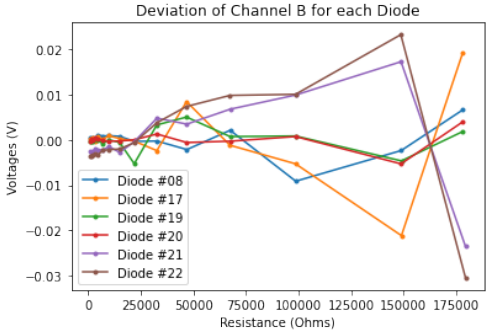

(b) Diode's Deviations on Channel B

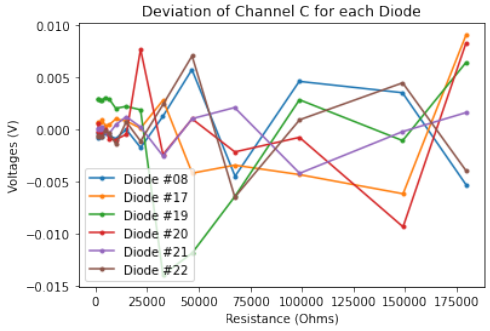

(c) Diode's Deviations on Channel C

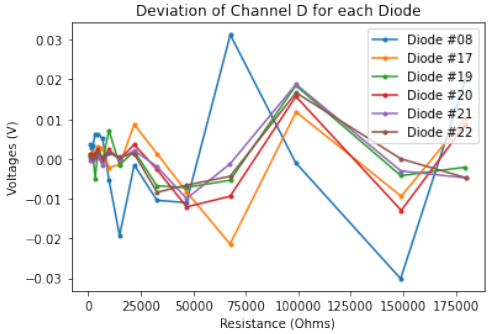

(d) Diode's Deviations on Channel D

Figure 17: Each Diodes' Deviations on each Channel

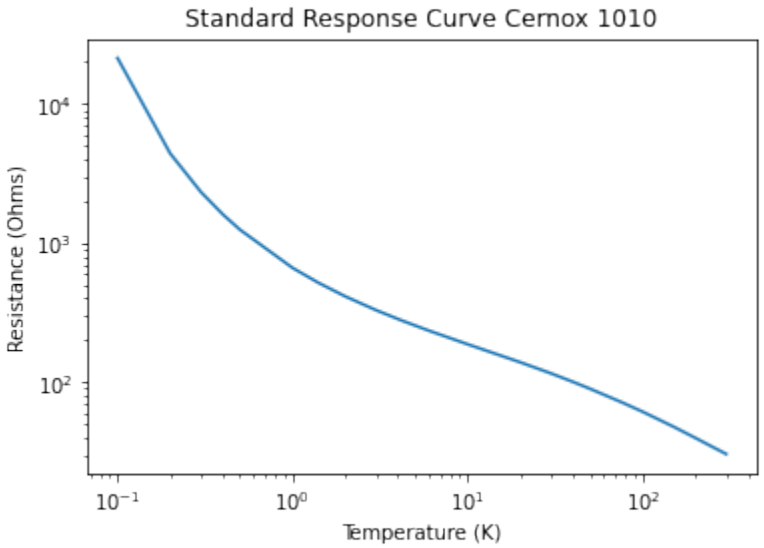

Figure 18: Standard Response Curve Cernox 1010

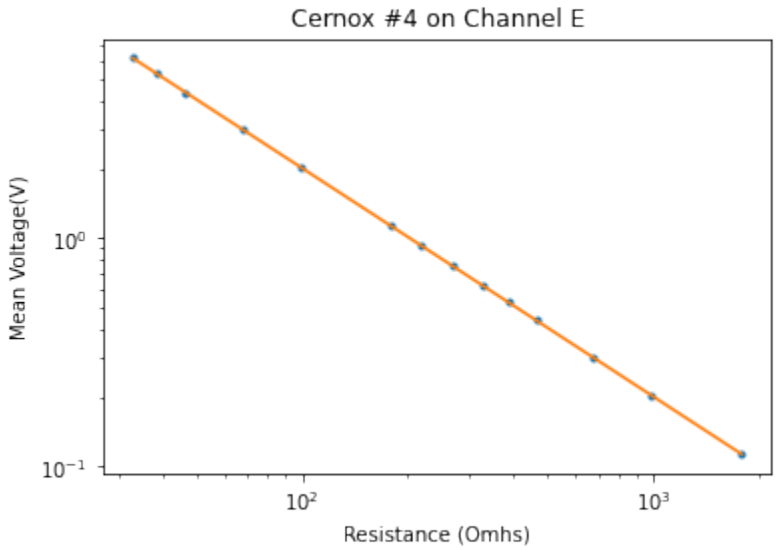

Figure 19: Data and model fit for Cernox 4 on Channel E

daughter card with a different model due to the difference in behavior of the Cernox daughter card to the diode daughter card. Once the measurements of the resistors and the mean output voltage was collected we simply plotted the data for the Cernox daughter card as Mean Voltage vs Resistance. Then you'd be able to see that the Cernox daughter card has a $\frac{1}{R}$ dependence the mean voltage output. We can then use a model to fit this data as shown in Figure 19. Note, Figure 19 has both axis as a logarithmic scales. The general model used is written as

$$V_{out} = \frac{\alpha}{R} + \beta \tag{42}$$

We will use the Chi-Square test the same way as the diode daughter card by assuming "goodness of fit" to extract the uncertainties in the voltage measurements. We are using the fluctuations of the data around the model to estimate the error on the data. We then use the general χ^2 equation written in Equation 15 to write χ^2 for the Cernox daughter card.

$$\chi^2 = \sum \frac{(V_i - \frac{\alpha}{R_i} - \beta)^2}{\sigma_V^2} \tag{43}$$

Where again,

$$\begin{aligned} V_i &= \textit{mean output voltage measured for each resistor.} \\ R_i &= \textit{the measured resistance for each resistor.} \\ \sigma_V &= \textit{the uncertainty of the output voltage.} \end{aligned}$$

We have found the best fit parameters, α and β, by fitting our data to our general model in Equation 42. For this specific Cernox, our model with the calculated best fit parameters is

$$\alpha = 202.2AR^2 \tag{44}$$

$$\beta = -.0003267V \tag{45}$$

All of the other α and β values can be found in Appendix 5 and 6.

α has units of amps times resistance squared. With out best fit parameter, we want to estimate the uncertainty in the output voltage by assuming that the minimum value of χ^2 . To do that we set χ^2 equal to the degrees of freedom subtracted by the number of model parameters. In this case, the degrees of freedom is the number of resistors tested which is 14 resistors so the minimum χ^2 is

$$\chi^2_{min} = \sum \frac{(V_i - \frac{\alpha}{R_i} - \beta)^2}{\sigma_V^2} = 12 \tag{46}$$

Thus, the uncertainty in the output voltage measurement is

$$\sigma_V = \sqrt{\frac{(V_i - \frac{\alpha}{R_i} - \beta)^2}{12}} \tag{47}$$

The uncertainty for our example is approximately

$$\sigma_V = \sqrt{\frac{(V_i - \frac{.2022}{R_i} + .0003265)^2}{12}} = .002152V \tag{48}$$

The goal of this project is the same as the diode daughter card and fundamentally is done in the same way. It's to test the need of attention for the calibration of these Cernox daughter cards to ensure proper temperature measurements of the cryostat. We need to propagate the error estimates on the voltages calculated above to compute the uncertainty in α and β. Then we can use that to get the uncertainties on the temperature measurements of these Cernox daughter cards. Again, We use the Hessian and the Fisher Information to accomplish this.

4.2.2 Calculating the Uncertainties on α and β

We will begin by calculating the Hessian for our Cernox daughter card shown as

$$H = 2 \begin{bmatrix} \sum \frac{1}{(R_i \sigma_V)^2} & \sum \frac{1}{R_i \sigma_V^2} \\ \sum \frac{1}{R_i \sigma_V^2} & \frac{N}{\sigma_V^2} \end{bmatrix} \tag{49}$$

To know the uncertainty of α and β we simply just need to calculate the inverse of the Hessian (Equation 24) for the Cernox daughter card is written as

$$\sigma_\mu = \frac{1}{2} \frac{1}{(\sum \frac{1}{(R_i \sigma_V)^2})(\frac{N}{\sigma_V^2}) - (\sum \frac{1}{R_i \sigma_V^2})^2} \begin{bmatrix} \frac{N}{\sigma_V^2} & -\sum \frac{1}{R_i \sigma_V^2} \\ -\sum \frac{1}{R_i \sigma_V^2} & \sum \frac{1}{(R_i \sigma_V)^2} \end{bmatrix} \tag{50}$$

The uncertainty on α is the first diagonal entry of the inverse Hessian.

$$\sigma_\alpha = \frac{1}{2} \frac{1}{(\sum \frac{1}{(R_i \sigma_V)^2})(\frac{N}{\sigma_V^2}) - (\sum \frac{1}{R_i \sigma_V^2})^2} (\frac{N}{\sigma_V^2}) \tag{51}$$

The calculated results for our example Cernox daughter card is

$$\sigma_\alpha = .001023AR^2 \tag{52}$$

The uncertainty on β is the second diagonal entry of the inverse Hessian.

$$\sigma_\beta = \frac{1}{2} \frac{1}{(\sum \frac{1}{(R_i \sigma_V)^2})(\frac{N}{\sigma_V^2}) - (\sum \frac{1}{R_i \sigma_V^2})^2} \sum \frac{1}{(R_i \sigma_V)^2} \tag{53}$$

The calculated results for the example Cernox is

$$\sigma_\beta = 1.792 * 10^{-7} V \tag{54}$$

All of the other σ_α and σ_β values can be found in Appendix 7 and 8.

4.2.3 Calculating the Uncertainties on the Temperature Measurement

Recapping on what we have accomplished so far. First, we assumed best fit for $\chi 2$ to estimate the errors on the measured voltage outputs associated with individual resistors for each of the Cernox daughter cards. Then we propagated those errors to calculate the errors associated with the gain (α) and offset voltage (β) by calculating the inverse Hessian matrix. Lastly, we want to calculate the errors on the temperature measurement for each Cernox Thermistor assuming the standard response curve (Figure 18) of the Cernox 1010. We accomplish this by computing the Fisher Information. Again the general formula was given in Equation 30. So first we need to compute the Jacobian for the Cernox thermistor from Equation 32. Since, the general temperature function in Equation 41 is a function of resistance we need to rewrite Equation 42 for resistance shown as

$$R_{cal} = \frac{\alpha}{(V_{out} - \beta)} \tag{55}$$

Next, need to use of the chain rule so we then can find how the temperature changes with each parameter, μ.

$$\frac{\partial T}{\partial \mu} = \frac{\partial T}{\partial R_{cal}} \frac{\partial R_{cal}}{\partial \mu} \tag{56}$$

Now we can compute the chain rule and complete the Jacobian for the Cernox which is given as

$$J = \frac{\partial T}{\partial R_{cal}} \begin{bmatrix} \frac{1}{(V_{out}-\beta)} \\ \frac{\alpha}{(V_{out}-\beta)^2} \end{bmatrix} \tag{57}$$

Substituting, Equation 42 for V_{out} so our Jacobian is completely in terms of R_i results in

$$J = \frac{\partial T}{\partial R_{cal}} \frac{1}{\alpha} \begin{bmatrix} \sum R_i \\ \sum R_i^2 \end{bmatrix} \tag{58}$$

This shows us how the temperature changes when each parameter, α and β, are altered. Notice that both rates of change depends on the slope of the standard response curve of the Cernox and the bias current. They both also inversely depend on α. The difference is that the Jacobian for β has an additional factor of resistance.

With the Jacobian (Equation 58) and the Hessian (Equation 49) for the Cernox daughter card, we can now construct the Fisher Information shown as

$$F_T = \frac{1}{(\frac{\partial T}{\partial R_{cal}})^2} \frac{2\alpha^2}{\sigma_V^2} \begin{bmatrix} \frac{1}{\sum R_i} & \frac{1}{\sum R_i^2} \end{bmatrix} \begin{bmatrix} \sum \frac{1}{R_i^2} & \sum \frac{1}{R_i} \\ \sum \frac{1}{R_i} & N \end{bmatrix} \begin{bmatrix} \frac{1}{\sum R_i} \\ \frac{1}{\sum R_i^2} \end{bmatrix} \tag{59}$$

$$F_T = (\frac{1}{(\frac{\partial T}{\partial R_{cal}})^2} \frac{2\alpha^2}{\sigma_V^2})(\sum \frac{1}{R_i^2} \frac{1}{(\sum R_i)^2} + \sum \frac{2}{R_i} \frac{1}{(\sum R_i)^3} + \frac{N}{(\sum R_i)^4}) \tag{60}$$

Where N is the number of data points. To solve for the uncertainty in temperature, σ_{Temp}, we simply use Equation 39. We can now calculate the uncertainty in the temperature measurements of a Cernox daughter cards as a function of temperature. For this particular Cernox daughter card, we calculated the uncertainty for the range of temperatures .1K to 1.4K shown in Figure 20. We chose this temperature range because this is the operating range for the Cernox in the cryostat. Using data similar to Section 3.2.4, we find that we want our uncertainty at 250mk to be about 2mk.

4.3 Results

As stated above we did this analysis for 10 different Cernox daughter cards on 3 different channels. We will now analyze data comparing a single Cernox daughter card on each different channel. Then we will compare

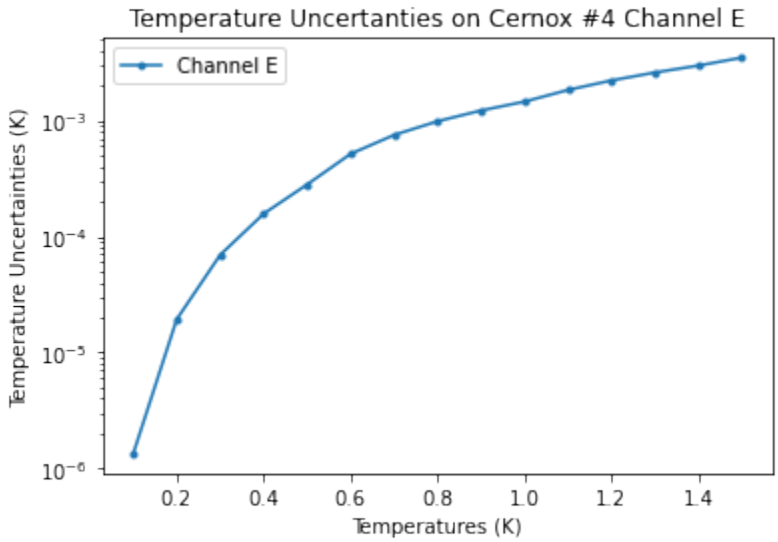

Figure 20: Temperature Uncertainty for Diode 08 from the Temperature ranges of .1K to 1.4K

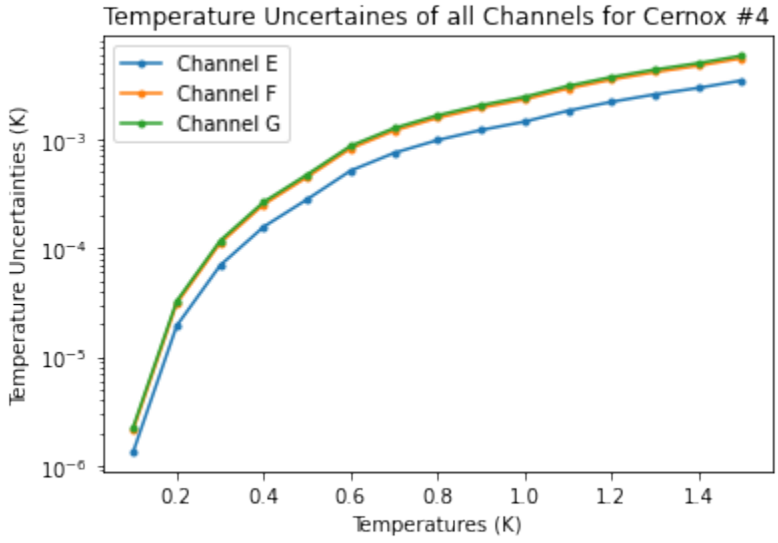

Figure 21: Temperature Uncertainties for each channel on Cernox 4

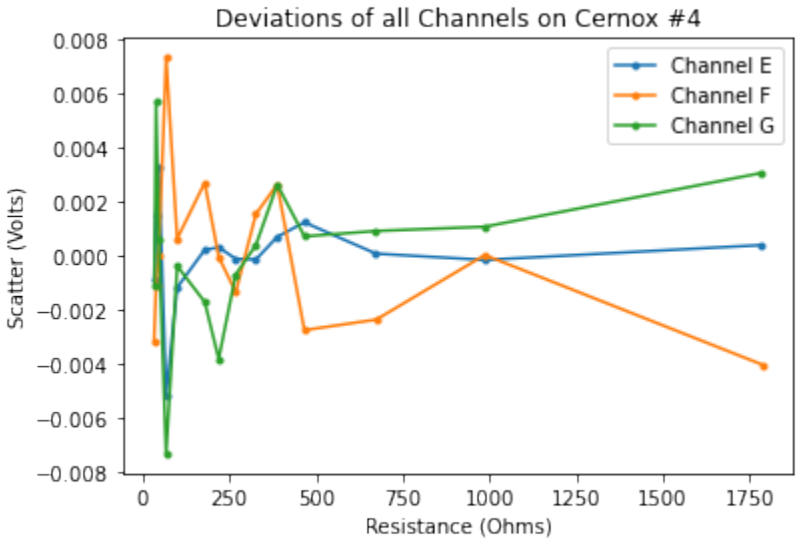

Figure 22: Deviation Comparison for Cernox 4 for all Channels

all the Cernox daughter cards on a single channel. First, we will examine a single Cernox daughter card on each different channel and we will continue our example above shown in Figure 21.

Again, we don't have a reason to believe that the temperature uncertainty on one channel should be substantially larger than another or the temperature uncertainty for one diode daughter card should be substantially larger that another. In Figure 21, we actually see that these measurement align pretty well. In addition to that our uncertainty is well below the 2mk estimate that we wanted. But we can still calculate the variations by using Equation 42 and finding the best fit parameters for each channel. We can then find the difference between the observed data and the model fitting of this data to compute the deviations for each channel shown as

$$\Delta V = V_i - \frac{\alpha}{R_i} - \beta \tag{61}$$

We do this to see if there are outlying data points however we can confidently assume that there are no drastic variations. So, we can plot these deviations against our resistance values to view the scatter of each channel which is represented in Figure 22.

Figure 22 doesn't demonstrate any cause for concern as the deviations are small. I show the computational results of each separate Cernox daughter card for all the channels tested in Figure 23.

We see that these measurements are successful at hitting the target uncertainty of 2mK in addition to no major deviations from channel to channel. So we go through the same process of calculating the deviations of the data and model presented in Figure 17. Again, we see that there are no concerns about these deviations.

Again, let's look at the same data in a different light. Let's now use the same computations for temperature uncertainty comparing each Cernox to a single channel which is shown in Figure 25.

Something that you might notice from Figure 25 is that the Cernox daughter cards 25, 34 and 35 seem to have higher uncertainty than any other Cernox daughter card. This is because these are Allan-Bradely Cernox daughter cards and they are generally more noisy. [8] We will then use the calculated deviations from Equation 61 to reorganize our data to compare the performance of a singular channel for each Cernox daughter card shown in Figure 24.

Through and through it seems that the calibration of these Cernox daughter cards were successful and seem to require less attention to calibrate. Every Cernox daughter card has hit our desired error uncertainty of 2mK at 250mK.

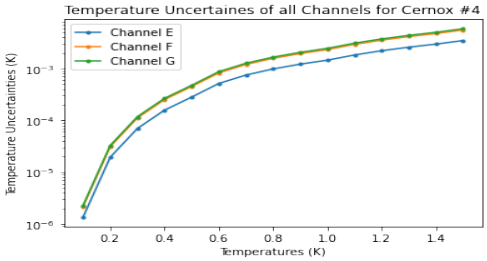

(a) Temperature Uncertainties for Cernox 4

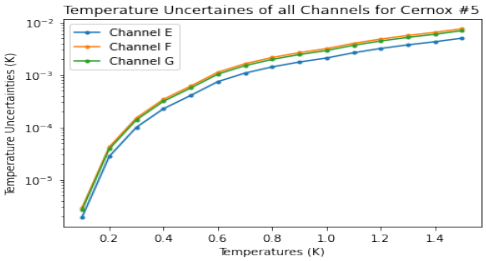

(b) Temperature Uncertainties for Cernox 5

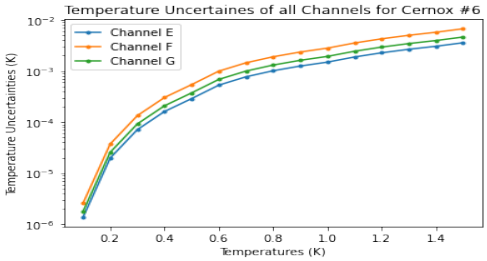

(c) Temperature Uncertainties for Cernox 6

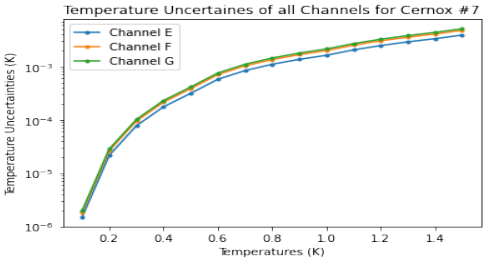

(d) Temperature Uncertainties for Cernox 7

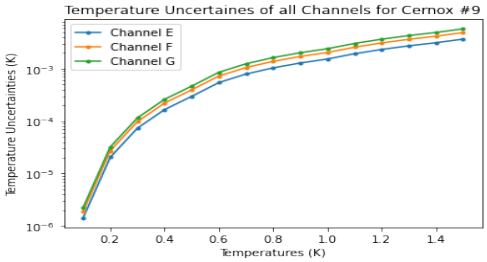

(e) Temperature Uncertainties for Cernox 9

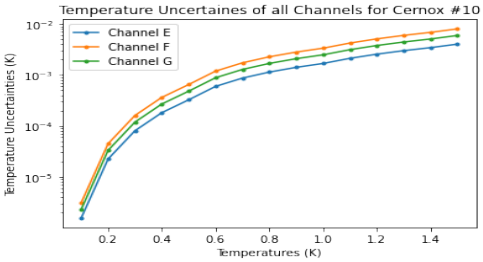

(f) Temperature Uncertainties for Cernox 10

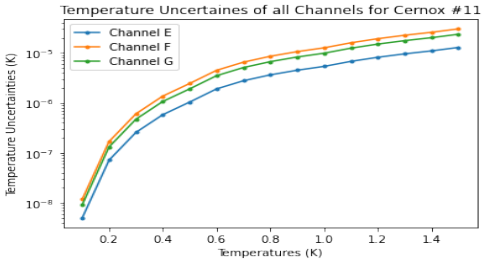

(g) Temperature Uncertainties for Cernox 11

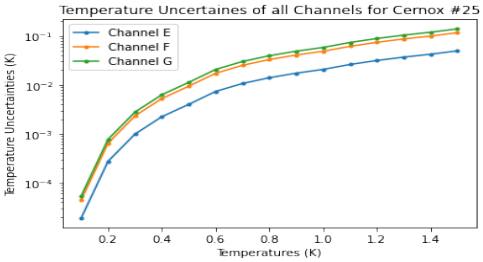

(h) Channel's Temperature Uncertainties for Cernox 25

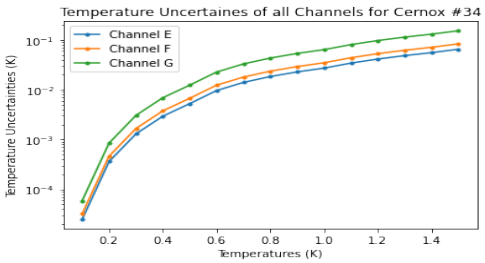

(i) Temperature Uncertainties for Cernox 34

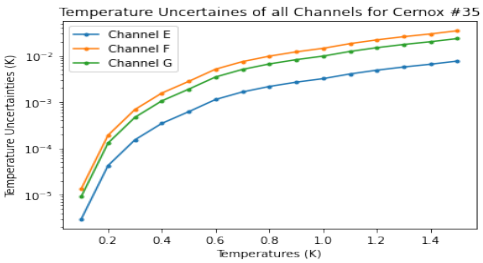

(j) Temperature Uncertainties for Cernox 35

Figure 23: Each Cernox Temperature Uncertainties for each Channel

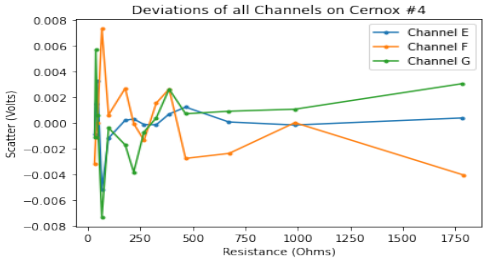

(a) Deviations for Cernox 4

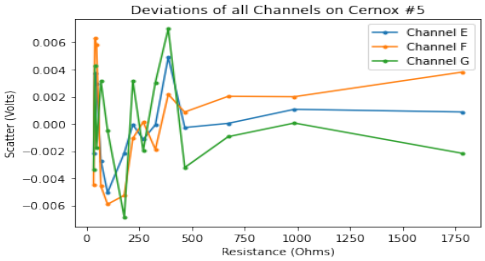

(b) Deviations for Cernox 5

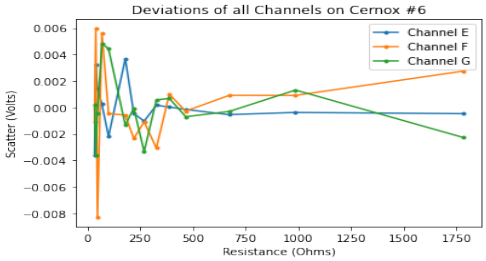

(c) Deviations for Cernox 6

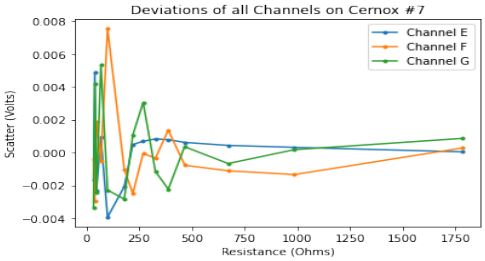

(d) Deviations for Cernox 7

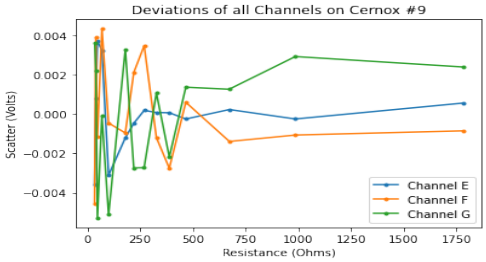

(e) Deviations for Cernox 9

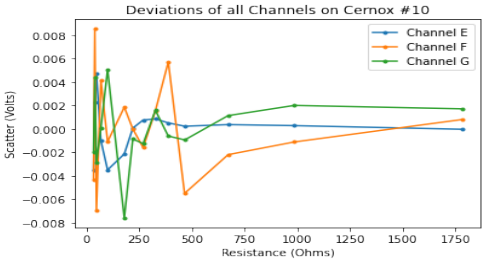

(f) Deviations for Cernox 10

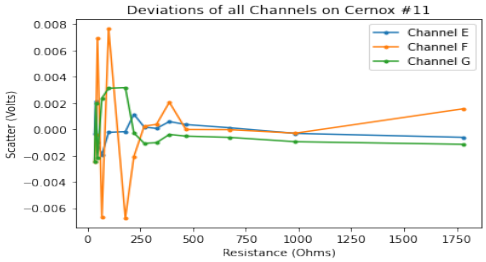

(g) Deviations for Cernox 11

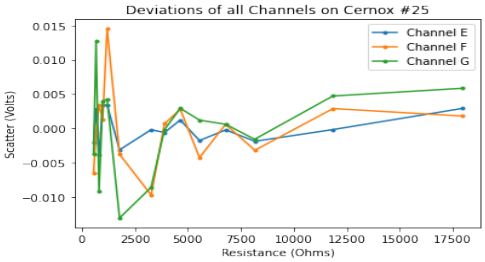

(h) Deviations for Cernox 25

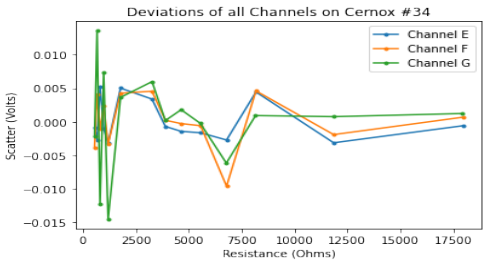

(i) Deviations for Cernox 34

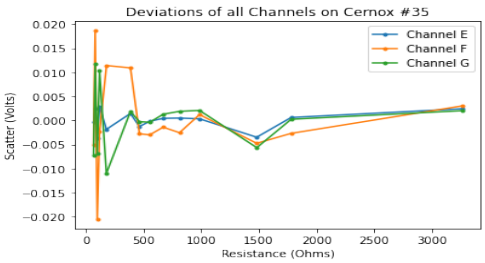

(j) Deviations for Cernox 35

Figure 24: Each Cernox Deviations for each Channel

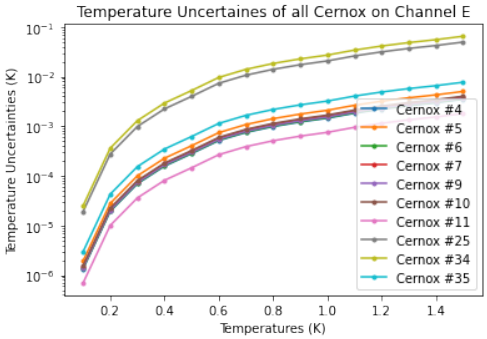

(a) Cernox Temperature Uncertainties on Channel E

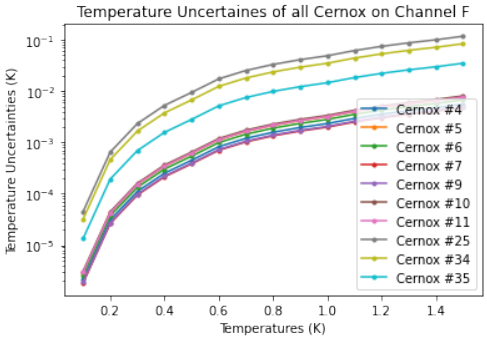

(b) Cernox Temperature Uncertainties on Channel F

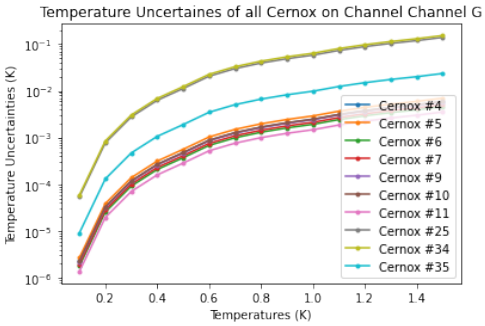

(c) Cernox Temperature Uncertainties on Channel G

Figure 25: Each Channel's Temperature Uncertainties for each Cernox

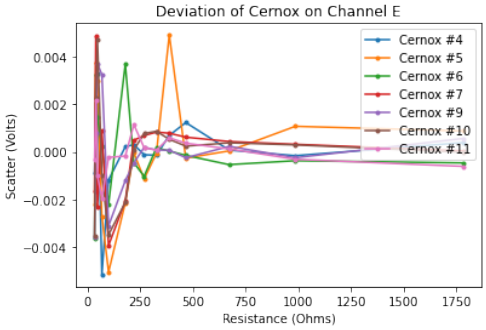

(a)Cernox Deviations on Channel E

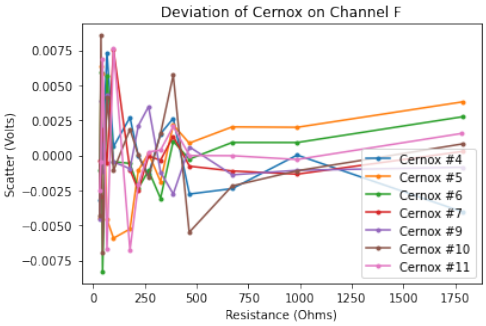

(b)Cernox Deviations on Channel F

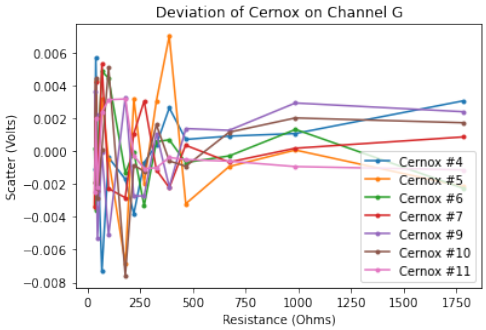

(c)Cernox Deviations on Channel G

Figure 26: Each Channel Deviations for each Cernox

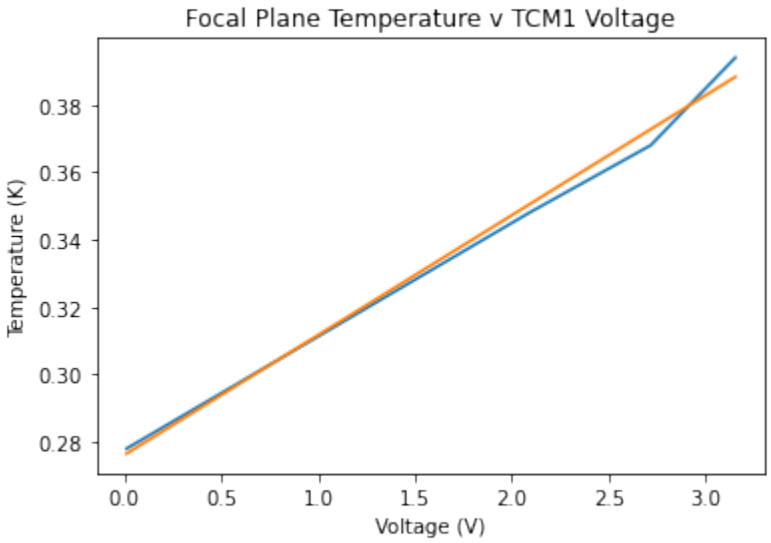

Figure 27: Calibration data and model fit

5 Neutron Transmutation Doped Germanium

In this chapter we will discuss the calibration and testing analysis of the Neutron Transmutation Doped Germanium Thermistor (NTD). We want to see the noise performance of the thermometers in the BA2 cryostat that will eventually replace a receiver from the KECK array in the current BA. The NTDs that we tested are located in the Temperature Control Modules (TCM). Two TCMs were attached to the focal plane and two TCMs were attached to the Ultra Cold (UC) strap on the dirty side. The way that the NTDs are biased and readout from the HS requires the NTDs need to be tuned by hand. I received the calibration data where they did this tuning in the BA2 cryostat. Once the NTDs are calibrated, we can then use test data from the BA2 cryostat to see if the performance of the NTDs are good. We want to know how the noise of the NTDs compare when the TCM is off to when it is turned on. Also, we want to compare the performance of the NTDs in BA1 to BA2 to ensure proper function.

5.1 NTD Calibration

First, we must calibrate our NTDs. They obtained the calibration data by cooling the focal plane to about 250mK which is readout by a Cernox and then tuned the NTDs. Next, they applied power to UC heaters to increase the temperature by approximately 30mK in three steps with one hour settle time for each step. The readout of the NTDs are voltages (V) where as the Cernox readout is temperature (K). I received calibrating data for the NTDs from run BA2.7. We can use this calibration data to write an equation for temperature as a function of voltage. We simply use a linear model to fit the data received from BA2.7 and use that fitted linear function to convert the voltage data from the NTDs in BA2 to temperature data in Kelvins. Resulting in an equation generally shown as

$$T = \alpha V + \beta \tag{62}$$

Example of the data and fit is shown in Figure 27. The fit is not exact but will be sufficient for the calibration.

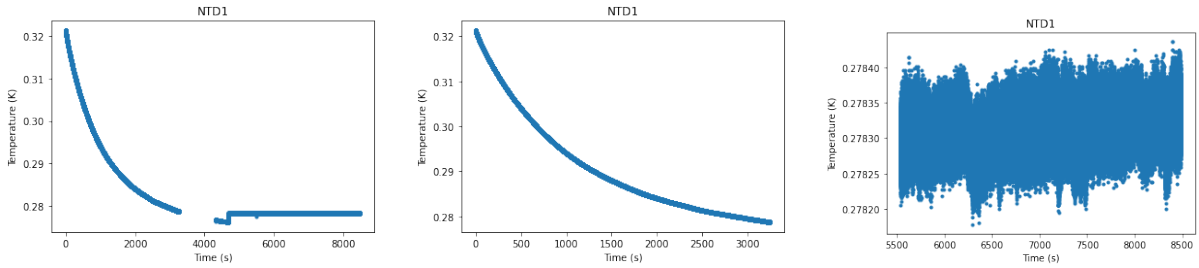

(a) Full NTD data (b) NTD data when TCM is off (c) NTD data when TCM is on

Figure 28: Division of NTD data from when TCM is off and on

5.1.1 NTD Noise

Now that we have the NTDs calibrated we can test their noise performance by using data from BA2. The goal is to calculate the power spectrum density of each NTD from BA2. I will demonstrate this with a single NTD and then show the results from each of the four NTDs.

First, we used our calibration function to convert our NTD data from voltages to temperature as shown in Figure 28. Figure 28a shows the full length of the collected data from BA2. Figure 28b shows the period of time when the TCM is off and Figure 28c shows the period of time when the TCM is turned on.

We want to calculate the Power Spectrum Density (PSD) so we need to go from time ordered data to frequency ordered data thus, we will need to use the Fast Fourier Transform (FFT). The FFT assumes that the time ordered data continues to infinite time so it infinitely loops our discrete data set. However, if you look at Figure 28b specifically, this would be an issue since the graph follows a trend at which do not start and end at approximately the same location. Thus, we would need to de-trend and window both data sets before calculating the FFT and the PSD.

First, we start by modeling our data where the TCM is turned off by using a 5th order polynomial which seems to fit our data well. Then we de-trend our data by subtracting our model from the data shown as

$$\Delta T_{off} = data - model \tag{63}$$

We then take the variations of both data sets and use a Hanning window function to ensure that the start and end points are zero. This allows us to properly use the FFT on the variations of the data sets. We then use the FFT to change from time ordered data to frequency ordered data. With the FFT, we can then calculate the PSD which is the absolute value of the FFT squared shown as

$$P = ||F||^2 \tag{64}$$

However, we want to normalize our PSD. To do that we need to backtrack slightly. We have collected data from the NTDs and performed a FFT. Our FFT data has a maximum frequency. The sampling rate, f_s, is the number of data points taken per second. To avoid aliasing, we define a term called the Nyquist Frequency, f_c, which is the point at which aliasing begins to occur. The Nyquist Frequency is the sample frequency divided by two or the inverse of twice the difference in time samples, Δt.[7] The Nyquist Frequency is shown below

$$f_c = \frac{f_s}{2} = \frac{1}{2\Delta t} \tag{65}$$

For our NTDs the Nyquist frequency is 100Hz. This is important because we want to calculate the normalized PSD. The normalization PSD can be calculated as the product of the PSD and the frequency resolution. The frequency resolution is the minimum change in frequency that the FFT can detect. [7]The frequency resolution can be defined as

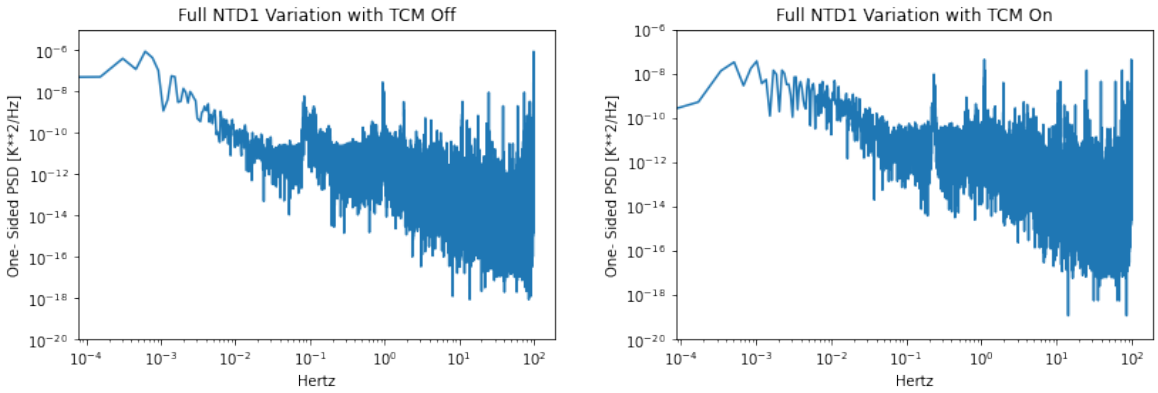

(a) Variation with TCM off

(b) Variation with TCM on

Figure 29: Variation of NTD data from when TCM is off and on

$$f_{Res} = \frac{f_s}{N} = \frac{1}{\Delta f N} \tag{66}$$

Thus, our normalized PSD turns out to be

$$P_{Norm} = \frac{2P}{\Delta f N^2} \tag{67}$$

The Δf is the change in frequency from evenly spaced frequencies from 0 to the Nyquist Critical Frequency in increments of the length of the data. There is a couple of things to notice in this. There is an extra factor of 2 due to calculating the One-Sided Power Spectrum from aliasing. Also, there is an extra factor of "N" and this is due to the specific FFT algorithm used for the computation. Once we perform these calculations for each set of data for when TCM is off and TCM is on can be shown in Figure 29 and the comparison of the two can be shown in Figure 30.

5.2 Results

Now, we can do the analysis for all four NTDs that were tested and see the results in Figure 31. You can see that the data from before and after the TCM was turned on are comparable and follow the same shape.

Next we can compare our calculated results in Figure 31 to BA1 results in Figure 32. Now in Figure 32 we will only be focusing on the PSD graph and from that graph we will have our attention on the BA receiver (the blue line). A thing to note is that our data has a bit more range of frequency and PSD. However, comparing the range of data from BA1 to BA2 we can see that they match well. They have a similar shape and have similar ordered pair of points. In the shape they both tend to decrease at first, flatten out and then decrease again. Now, you might note that the there is more deviations in the PSD in BA2 that BA1 based off of visuals. The reason for this is a slight difference in the calculation of the PSD. They had averaged points together which decreases the deviations within the PSD figure. Overall, we can conclude that the functionality of the NTDs in BA2 is comparable to the functionality of BA1 which is a success.

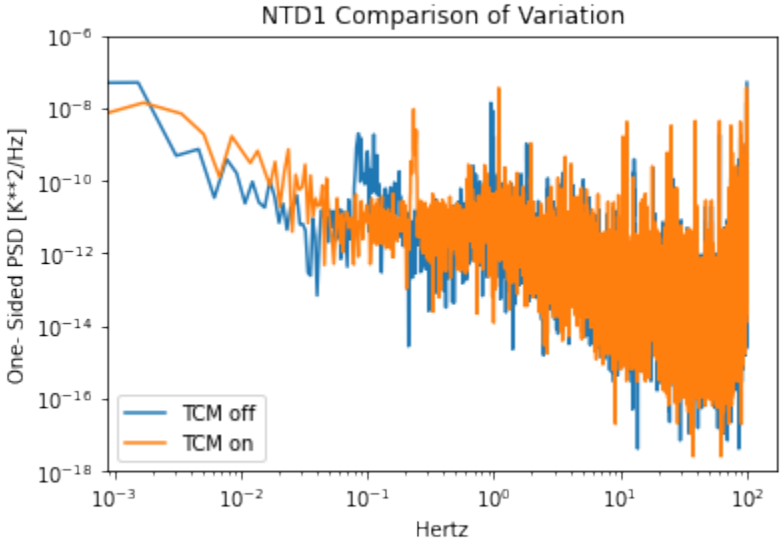

Figure 30: Comparison of the Variation of TCM off and on

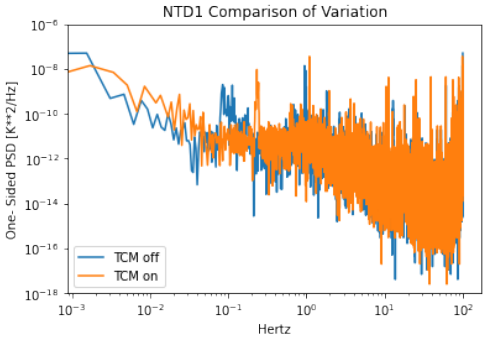

(a) NTD1 Comparison of TCM off and on

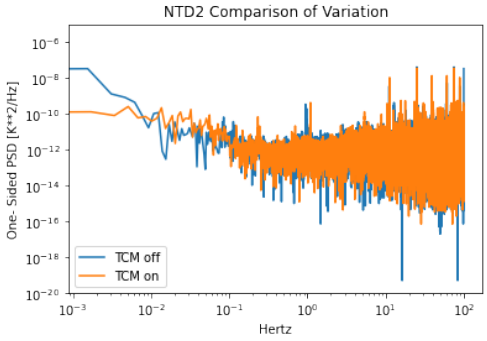

(b) NTD2 Comparison of TCM off and on

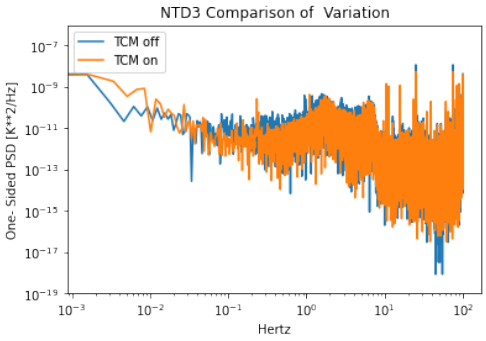

(c)NTD3 Comparison of TCM off and on

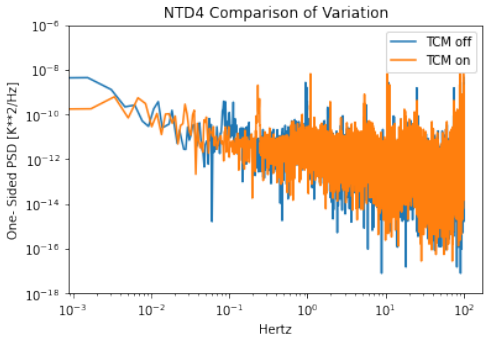

(d) NTD4 Comparison of TCM off and on

Figure 31: Each NTDs Noise Comparison on when TCM is turned off and on.

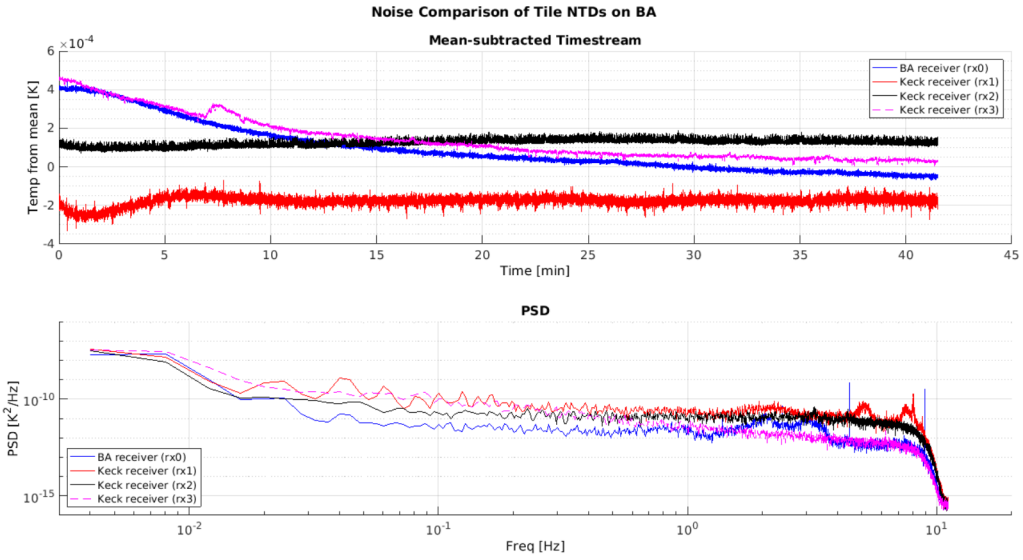

Figure 32: Noise Comparison of Tile NTDs on BA. For this thesis we only focuse on the PSD and the BA receiver portion of the graph. [6]

Appendix

α (Amps) Estimates for Diode Daughter Cards (DC)						
	Diode DC 8	Diode DC 17	Diode DC 19	Diode DC 20	Diode DC 21	Diode DC 22
Channel A	$4.032 * 10^{-5}$	$4.018 * 10^{-5}$	$4.035 * 10^{-5}$	$4.033 * 10^{-5}$	$4.025 * 10^{-5}$	$4.034 * 10^{-5}$
Channel B	$4.010 * 10^{-5}$	$4.020 * 10^{-5}$	$4.019 * 10^{-5}$	$4.016 * 10^{-5}$	$4.009 * 10^{-5}$	$4.006 * 10^{-5}$
Channel C	$4.022 * 10^{-5}$	$4.016 * 10^{-5}$	$4.028 * 10^{-5}$	$4.021 * 10^{-5}$	$4.020 * 10^{-5}$	$4.021 * 10^{-5}$
Channel D	$4.058 * 10^{-5}$	$4.034 * 10^{-5}$	$4.045 * 10^{-5}$	$4.041 * 10^{-5}$	$4.032 * 10^{-5}$	$4.041 * 10^{-5}$

Table 1: All α Values for the Diode Daughter Cards.

β (V) Estimates for Diode Daughter Cards (DC)						
	Diode DC 8	Diode DC 17	Diode DC 19	Diode DC 20	Diode DC 21	Diode DC 22
Channel A	$-2.243*10^{-3}$	$-1.590*10^{-3}$	$-5.336*10^{-3}$	$-7.608*10^{-3}$	$-5.895*10^{-3}$	$-3.316*10^{-3}$
Channel B	$-8.351*10^{-4}$	$-8.026*10^{-3}$	$-3.474*10^{-3}$	$-5.348*10^{-4}$	$-6.967*10^{-3}$	$-3.606*10^{-4}$
Channel C	$-4.537*10^{-3}$	$-7.169*10^{-3}$	$-2.394*10^{-3}$	$-1.212*10^{-2}$	$-1.164*10^{-2}$	$-7.688*10^{-3}$
Channel D	$-4.672*10^{-3}$	$-1.759*10^{-3}$	$-4.749*10^{-3}$	$-8.410*10^{-3}$	$-6.041*10^{-3}$	$-3.546*10^{-3}$

Table 2: All β Values for the Diode Daughter Cards.

σ_α (Amps) Estimates for Diode Daughter Cards (DC)						
	Diode DC 8	Diode DC 17	Diode DC 19	Diode DC 20	Diode DC 21	Diode DC 22
Channel A	$5.399 * 10^{-9}$	$1.486 * 10^{-9}$	$8.650 * 10^{-9}$	$9.484 * 10^{-9}$	$5.226 * 10^{-9}$	$9.281 * 10^{-9}$
Channel B	$1.115 * 10^{-8}$	$2.803 * 10^{-9}$	$8.829 * 10^{-9}$	$6.340 * 10^{-9}$	$3.018 * 10^{-8}$	$3.912 * 10^{-8}$
Channel C	$1.115 * 10^{-8}$	$2.803 * 10^{-8}$	$8.829 * 10^{-9}$	$6.340 * 10^{-9}$	$3.018 * 10^{-9}$	$3.912 * 10^{-8}$
Channel D	$5.071 * 10^{-8}$	$2.854 * 10^{-8}$	$2.210 * 10^{-8}$	$2.530 * 10^{-8}$	$2.054 * 10^{-8}$	$1.929 * 10^{-8}$

Table 3: All σ_α Values for the Diode Daughter Cards.

σ_β (V) Estimates for Diode Daughter Cards (DC)						
	Diode DC 8	Diode DC 17	Diode DC 19	Diode DC 20	Diode DC 21	Diode DC 22
Channel A	$3.763 * 10^{-4}$	$1.037 * 10^{-3}$	$6.040 * 10^{-4}$	$6.620 * 10^{-4}$	$3.648 * 10^{-4}$	$6.480 * 10^{-4}$
Channel B	$7.739 * 10^{-4}$	$1.946 * 10^{-3}$	$6.132 * 10^{-4}$	$4.402 * 10^{-4}$	$2.102 * 10^{-3}$	$2.723 * 10^{-3}$
Channel C	$7.084 * 10^{-4}$	$8.603 * 10^{-4}$	$1.417 * 10^{-3}$	$9.693 * 10^{-4}$	$2.102 * 10^{-3}$	$2.723 * 10^{-3}$
Channel D	$3.532 * 10^{-3}$	$1.990 * 10^{-3}$	$1.544 * 10^{-3}$	$1.763 * 10^{-3}$	$3.753 * 10^{-4}$	$7.576 * 10^{-4}$

Table 4: All σ_β Values for the Diode Daughter Cards.

α (AmpsR^2) Estimates for Cernox Daughter Cards (DC)			
	Channel E	Channel F	Channel G
Cernox DC 4	202.0	202.2	202.9
Cernox DC 5	202.6	202.5	202.5
Cernox DC 6	202.4	202.5	202.2
Cernox DC 7	202.3	202.0	202.2
Cernox DC 9	202.5	201.6	203.9
Cernox DC 10	202.3	202.7	202.2
Cernox DC 11	202.0	202.4	202.3
Cernox DC 25	3693.9	3697.0	3695.4
Cernox DC 34	3603.0	3604.7	3611.9
Cernox DC 35	407.0	406.6	406.8

Table 5: All α Values for the Cernox Daughter Cards.

β (V) Estimates for Cernox Daughter Cards (DC)			
	Channel E	Channel F	Channel G
Cernox DC 4	$2.116 * 10^{-4}$	$-3.124 * 10^{-3}$	$-1.858 * 10^{-4}$
Cernox DC 5	$-6.595 * 10^{-3}$	$-2.390 * 10^{-3}$	$-5.522 * 10^{-4}$
Cernox DC 6	$-1.226 * 10^{-4}$	$-1.357 * 10^{-3}$	$7.598 * 10^{-4}$
Cernox DC 7	$4.833 * 10^{-4}$	$1.379 * 10^{-3}$	$1.710 * 10^{-4}$
Cernox DC 9	$-1.380 * 10^{-4}$	$3.752 * 10^{-3}$	$-2.792 * 10^{-4}$
Cernox DC 10	$1.443 * 10^{-3}$	$-4.523 * 10^{-3}$	$1.819 * 10^{-4}$
Cernox DC 11	$1.137 * 10^{-3}$	$-2.321 * 10^{-4}$	$1.541 * 10^{-4}$
Cernox DC 25	$1.745 * 10^{-4}$	$-8.895 * 10^{-4}$	$-1.843 * 10^{-4}$
Cernox DC 34	$3.092 * 10^{-3}$	$1.720 * 10^{-3}$	$-5.652 * 10^{-4}$
Cernox DC 35	$-2.167 * 10^{-3}$	$-6.442 * 10^{-4}$	$-1.654 * 10^{-4}$

Table 6: All β Values for the Cernox Daughter Cards.

σ_α (AmpsR^2) Estimates for Cernox Daughter Cards (DC)			
	Channel E	Channel F	Channel G
Cernox DC 4	$7.514 * 10^{-4}$	$1.923 * 10^{-3}$	$2.166 * 10^{-3}$
Cernox DC 5	$1.571 * 10^{-3}$	$3.581 * 10^{-3}$	$3.028 * 10^{-3}$
Cernox DC 6	$7.985 * 10^{-4}$	$2.791 * 10^{-3}$	$1.318 * 10^{-3}$
Cernox DC 7	$9.337 * 10^{-4}$	$1.400 * 10^{-3}$	$1.606 * 10^{-3}$
Cernox DC 9	$8.418 * 10^{-4}$	$1.481 * 10^{-3}$	$2.106 * 10^{-3}$
Cernox DC 10	$1.005 * 10^{-3}$	$4.017 * 10^{-3}$	$2.197 * 10^{-3}$
Cernox DC 11	$2.017 * 10^{-4}$	$3.639 * 10^{-3}$	$7.761 * 10^{-4}$
Cernox DC 25	$3.432 * 10^{-1}$	1.899	2.718
Cernox DC 34	$5.600 * 10^{-1}$	$9.202 * 10^{-1}$	3.120
Cernox DC 35	$3.857 * 10^{-3}$	$7.847 * 10^{-2}$	$3.613 * 10^{-2}$

Table 7: All σ_α Values for the Cernox Daughter Cards.

σ_β (V) Estimates for Cernox Daughter Cards (DC)			
	Channel E	Channel F	Channel G
Cernox DC 4	$1.316 * 10^{-7}$	$3.372 * 10^{-7}$	$3.718 * 10^{-7}$
Cernox DC 5	$2.752 * 10^{-7}$	$6.257 * 10^{-7}$	$5.305 * 10^{-7}$
Cernox DC 6	$1.382 * 10^{-7}$	$4.876 * 10^{-7}$	$2.309 * 10^{-7}$
Cernox DC 7	$1.635 * 10^{-7}$	$2.452 * 10^{-7}$	$2.807 * 10^{-7}$
Cernox DC 9	$1.472 * 10^{-7}$	$2.593 * 10^{-7}$	$3.614 * 10^{-7}$
Cernox DC 10	$1.759 * 10^{-7}$	$7.019 * 10^{-7}$	$3.849 * 10^{-7}$
Cernox DC 11	$3.532 * 10^{-8}$	$6.371 * 10^{-7}$	$1.359 * 10^{-7}$
Cernox DC 25	$2.282 * 10^{-7}$	$1.262 * 10^{-6}$	$1.809 * 10^{-6}$
Cernox DC 34	$3.728 * 10^{-7}$	$6.123 * 10^{-7}$	$2.073 * 10^{-6}$
Cernox DC 35	$1.630 * 10^{-7}$	$3.320 * 10^{-6}$	$1.528 * 10^{-6}$

Table 8: All σ_β Values for the Cernox Daughter Cards.

References

[1] Marc Kamionkowski and Ely D. Kovetz. "The Quest for B Modes from Inflationary Gravitational Waves". In: Annual Review of Astronomy and Astrophysics (September 2016), VOL: 54 PAGES: 227-269. DOI: 10.1146/annurev-astro-081915-02343. arXiv:1510.06042

[2] Ryden, Barbara. Introduction to Cosmology. Cambridge University Press, 2016.

[3] A. Schillaci et al. "Design and Performance of the First BICEP Array Receiver". IN: Journal of Low Temperature Physics, VOL: 199, PAGES: 3-4. DOI: 10.1007/s10909-020-02394-6, arXiv:2002.05228

[4] L. Moncelsi et al. "Receiver Development for BICEP Array, a Next-Generation CMB Polarimeter at the South Pole". IN: arXiv. DOI: 10.48550/ARXIV.2012.04047, arXiv:2012.04047

[5] L. Moncelsi. BICEP Array Internal Memo

[6] S. Palladino, 2021. "Constraining Primordial Gravitational Waves with BICEP/KECK Array Telescopes and Developing the BICEP Array Housekeeping System". PhD Thesis, University of Cincinnati, Cincinnati.

[7] Press, William, et al. "Numerical Recipes: The Art of Scientific Computing". Cambridge University Press, 2007.

[8] D. Goldfinger.Run BA3.5 Notes, BICEP Array Internal Memo

[9] Lakeshore Cryotronics. https://www.lakeshore.com/

[10] Mazumdar, Anupam. "Slow-roll inflation and the Hamilton-Jacobi Formalism." (2019).

[11] "Hunting Season for Primordial Gravitational Waves" https://physics.aps.org/articles/v13/164